

The effect of kick velocities on the spatial distribution of millisecond pulsars and implications for the Galactic center excess

Harrison Ploeg and Chris Gordon

School of Physical and Chemical Sciences, University of Canterbury, Christchurch, New Zealand

E-mail: hzp10@uclive.ac.nz, chris.gordon@canterbury.ac.nz

Abstract. Recently it has become apparent that the Galactic center excess (GCE) is spatially correlated with the stellar distribution in the Galactic bulge. This has given extra motivation for the unresolved population of millisecond pulsars (MSPs) explanation for the GCE. However, in the “recycling” channel the neutron star forms from a core collapse supernovae that undergoes a random “kick” due to the asymmetry of the explosion. This would imply a smoothing out of the spatial distribution of the MSPs. We use N -body simulations to model how the MSP spatial distribution changes. We estimate the probability distribution of natal kick velocities using the resolved gamma-ray MSP proper motions, where MSPs have random velocities relative to the circular motion with a scale parameter of 77 ± 6 km/s. We find that, due to the natal kicks, there is an approximately 10% increase in each of the bulge MSP spatial distribution dimensions and also the bulge MSP distribution becomes less boxy but is still far from being spherical.

Contents

1	Introduction	1
2	Method	2
3	Results	5
4	Discussion and Conclusions	7
A	Uniform kick rate, MWb, and MWc0.8 figures	20
B	Markov Chain Monte Carlo Method	21

1 Introduction

The Galactic Center Excess (GCE) is an extended source of gamma radiation in the central region of the Galaxy found in the Fermi Large Area Telescope (Fermi-LAT) data. When first discovered, its apparently spherically symmetric profile and spectrum peaking at a few GeV suggested that it may be evidence of self-annihilating weakly interacting massive particles (WIMPs) distributed according to a Navarro-Frenk-White (NFW) profile [1–4]. An alternative scenario that was proposed was one in which the GCE was produced by a population of unresolved millisecond pulsars (MSPs) [5]. More recently, evidence has suggested that in fact the GCE is not spherically symmetric but actually is correlated with the stellar mass in the Galactic bulge and so has a more boxy morphology [6–11]. Although one recent study, using different methods, still argues for a spherically symmetric GCE [12]. If the GCE does trace the stellar mass of the bulge this would favor the MSP (or other dim unresolved astrophysical point source) explanation. Additionally, several studies have claimed to find a non-Poissonian component to the GCE [13, 14] which may be further evidence for the MSP explanation. However, there is some controversy regarding the level of systematics in this approach [e.g., 11, 15–19].

In the “recycling” model of MSP formation a neutron star is spun up to millisecond periods through the transfer of mass from a binary companion. This requires that the binary system survives the kick produced by any asymmetry in the core collapse supernova explosion [20]. However, an alternative to the recycling channel is accretion induced collapse of white dwarfs into neutron stars which may produce more than half of all observed MSPs [21–24]. In this case the system does not receive a significant natal kick [25, 26]. This would imply that the MSPs have much smaller peculiar velocities in comparison to the recycling model [27–29].

Ploeg et al. [30] (hereafter referred to as P20) modelled Fermi-LAT detected MSPs as having a Maxwell distributed peculiar velocity with the scale parameter σ_v found to be $77 \pm 6 \text{ km s}^{-1}$ where we quote error bars at the 68% confidence interval throughout this article. This velocity applies for disk MSPs and we assume it will not be significantly different for bulge MSPs. Although the star formation histories are very different in the bulge and disk, as can be seen from Fig. 6 of P20 the probability distribution of luminosities in the bulge and disk only differ by a few percent. Also, as can be seen from Fig. 11 of P20, the bulge and disk have a ratio of number of MSPs formed per solar mass which is within one error bar of each other. Based on this, we assume that the bulge and disk have the same mix of MSP formation channels and thus the same probability distribution of natal kick velocities.

If the source of the GCE is a population of unresolved MSPs, then the spatial distribution may be smoothed to some degree relative to the stellar mass in the bulge. Eckner et al. [31] used the virial theorem to estimate the “smoothing length” of MSPs as 700 – 900 pc for kicks $\lesssim 70 \text{ km s}^{-1}$. However, they assumed a spherically symmetric spatial distribution for the MSPs.

In this article we use N -body simulations to estimate what are the effects of MSP kicks for a boxy bulge like distribution. In Section 2 we explain our method. Our results are given in Section 3, and our conclusions in Section 4.

2 Method

For this work we use the code of Bedorf et al. [32] to run N -body simulations in order to model the Milky Way.¹ We use parameters corresponding to initial conditions labelled MWa, MWb and MWc0.8 as denoted by Fujii et al. [33] as they were the initial conditions that led to the best fitting simulations to Galaxy observations that Fujii et al. found. The initial conditions consist of a parametric description of the dark matter halo, Galactic disk and bulge. Comparing to bulge kinematics, bar length, and pattern speed observations Fujii et al. found MWa was the initial conditions which gave the best fit to the data, followed by MWb, and then MWc0.8. For each initial condition model we generated a total of 30 million disk, bulge and dark matter halo particles. These initial populations are generated using the methods of Kuijken and Dubinski [34], Widrow and Dubinski [35], and Widrow et al. [36].² As in Fujii et al. [33], we use time-steps of ~ 0.6 Myr, an opening angle of 0.4 and ran the simulation for 10 Gyr. However, we use a softening length of 30 pc. Also, our dark-matter halo particles have a mass 8 times larger than the disk and bulge particles. Taking into account the masses of the various components, this implies that, out of the 30 million particles, approximately 10 million particles represent stellar mass and the remainder represent dark matter.

In order to model the density of MSPs, we additionally include massless (so they do not affect the simulation) disk and bulge particles that are given a normally distributed perturbation to each component of their velocity vector with mean zero and standard deviation σ_k . The kick velocity magnitude is therefore Maxwell distributed. The probability density function of a Maxwell distribution can be written as:

$$p(x) = \sqrt{\frac{2}{\pi}} \frac{x^2 \exp(-x^2/2\sigma^2)}{\sigma^3} \quad (2.1)$$

where x is the magnitude of a three dimensional vector with components sampled from the normal distribution $\mathcal{N}(0, \sigma^2)$. For each model we try a case where the kicks occurred at the beginning of the N -body simulations and a case where the kicks occur randomly with a uniform rate over the course of the 10 Gyr. These cases approximate scenarios in which MSPs are largely born early or at a relatively steady rate. From these two extremes, we can estimate the sensitivity of our results to the MSP age distribution.

The first step is to estimate the kick velocity scale required to produce a peculiar velocity distribution consistent with P20 where for the best model the peculiar velocity scale parameter was $\sigma_v = 77 \pm 6$ km s⁻¹. We do this by running each initial condition model with 41 populations of 10^5 kicked particles with σ_k between 70 and 110 km s⁻¹. We separate the velocity of each particle into two components:

$$\mathbf{v} = \mathbf{v}_c + \mathbf{v}_p \quad (2.2)$$

where \mathbf{v}_c is the velocity of a particle on a circular orbit around the center of the galaxy and \mathbf{v}_p is the peculiar velocity. The magnitude of \mathbf{v}_c for a particle with coordinates x , y , and z can be evaluated using the centripetal force:

$$\|\mathbf{v}_c\| = \sqrt{\|\mathbf{a}_c(x, y, 0)\| R} \quad (2.3)$$

where $\mathbf{a}_c(x, y, z)$ is the acceleration toward the center of the galaxy which can be obtained from a small modification to the N -body code and $R^2 = x^2 + y^2$. For R outside the bulge region, and for small peculiar velocity, we are therefore assuming that particles are rotating with the disk, with \mathbf{v}_c the rotation velocity of the disk at R [37].

We use a maximum likelihood estimate of the final σ_v for each initial σ_k . For a set of N particles with peculiar velocities v_1, \dots, v_N , the log-likelihood is obtained by assuming velocities have a Maxwell distribution:

$$\log(L) = \frac{N}{2} \log\left(\frac{2}{\pi}\right) - 3N \log(\sigma_v) + \sum_{i=1}^N 2 \log(v_i) - \frac{v_i^2}{2\sigma_v^2} \quad (2.4)$$

and therefore

$$\frac{d \log(L)}{d \sigma_v} = -\frac{3N}{\sigma_v} + \sum_{i=1}^N \frac{v_i^2}{\sigma_v^3}. \quad (2.5)$$

¹Available at: <https://github.com/treecode/Bonsai>

²We used the implementation at: <https://github.com/treecode/Galactics.parallel>

Then solving for σ_v where $d \log(L)/d\sigma_v = 0$, we find the maximum likelihood estimate for σ_v is:

$$\hat{\sigma}_v = \sqrt{\frac{\sum_{i=1}^N v_i^2}{3N}} \quad (2.6)$$

This is done for particles where $4 \text{ kpc} \leq R \leq 12 \text{ kpc}$ and $|z| \leq 2 \text{ kpc}$, ensuring we are estimating the peculiar velocity distribution scale parameter for particles in the disk region from which gamma-ray MSPs are most likely to be resolved and where v_c approximately represents disk rotation.

Once we have a best fitting σ_k we use that σ_k to generate an additional population of kicked particles. We rerun the N -body simulations for each set of initial conditions (MWa, MWb, MWc0.8) including in each initial condition case two new populations of massless particles where each new population has 2×10^6 particles. These new populations are made massless so as not to influence the gravitational potential of the N -body simulation. The first massless population is sampled from the initial condition model. For the second population we duplicate the first population and then add a Maxwell distributed kick with scale parameter σ_k at the beginning of the simulation to each particle in the second population. The simulations are then run for 10 Gy to see what the final state of the two massless populations is for each set of initial conditions. We then repeat this process but instead of the second population having a Maxwell distributed kick added at the beginning of the simulation we add it randomly to members of the second population at a uniform rate throughout the simulation. So in the end for each initial condition we have two massless populations of unkicked particles, one massless population of particles kicked at the beginning and one for particles kicked at a uniform rate throughout the simulation. We used two populations of massless unkicked particles to make the kicked at beginning cases and uniform kick rate cases as independent as possible from each other.

In order to understand the effect of MSP kicks on the final spatial distribution of MSPs we found it clearer to have a parametric description of the spatial distribution. Then by comparing the parameters for the kick and no-kick cases we can have a succinct way of characterising the effects of the kicks. We use Markov Chain Monte Carlo (MCMC) to fit the parametric model to both final particle distributions. The form of our parametric model for the final spatial distribution of MSPs was chosen based on previous studies and also such that there were not excessive residuals between the model fits and the simulations. Our model of the final distributions consists of four components: a spherically symmetric bulge, a potentially non-spherical bulge also known as a bar, a long bar and a disk. The spherically symmetric bulge component uses the Hernquist model [38]:

$$\rho_{\text{Hernquist}}(r) \propto \frac{1}{(r/a_b)(1+r/a_b)^3} \quad (2.7)$$

where $r^2 = x^2 + y^2 + z^2$ and a_b is a free parameter. Our initial conditions models, based on those of Fujii et al. [33], also include a component distributed according the Hernquist model which would naturally have different parameter values to the one we fitted after 10 Gy of evolution. Our bar model is distributed as:

$$\rho_{\text{bar}}(R_s) \propto K_0(R_s) \times \begin{cases} 1 & R \leq R_{\text{end}} \\ \exp(-(R - R_{\text{end}})^2/h_{\text{end}}^2) & R > R_{\text{end}} \end{cases} \quad (2.8)$$

where K_0 is the modified Bessel function of the second kind and where:

$$R_s = \left(R_{\perp}^{C_{\parallel}} + \left(\frac{|z|}{z_b} \right)^{C_{\parallel}} \right)^{1/C_{\parallel}} \quad (2.9)$$

$$R_{\perp} = \left(\left(\frac{|x|}{x_b} \right)^{C_{\perp}} + \left(\frac{|y|}{y_b} \right)^{C_{\perp}} \right)^{1/C_{\perp}}. \quad (2.10)$$

The free parameters are C_{\parallel} , C_{\perp} , x_b , y_b , z_b and R_{end} with h_{end} fixed at $\sqrt{1/2}$ kpc. The effective radius is R_s ; the scale lengths are x_b , y_b , and z_b ; and C_{\perp} and C_{\parallel} are the face-on and edge-on shape parameters. The bar shape is elliptical in the corresponding direction when $C_{\perp}, C_{\parallel} = 2$, diamond-shaped when $C_{\perp}, C_{\parallel} < 2$, and boxy when $C_{\perp}, C_{\parallel} > 2$. The Gaussian function with scale length h_{end} in Eq. (2.8) truncates the bar at radius R_{end} . The modified Bessel function

was also used in Cao et al. [39] to model the distribution of red clump giants, but with no cutoff and with $C_{\parallel} = 4$ and $C_{\perp} = 2$. For the long bar we use [40]:

$$\rho_{\text{long bar}}(x, y, z) \propto \exp \left(- \left(\left(\frac{|x|}{x_{\text{lb}}} \right)^{C_{\perp, \text{lb}}} + \left(\frac{|y|}{y_{\text{lb}}} \right)^{C_{\perp, \text{lb}}} \right)^{1/C_{\perp, \text{lb}}} \right) \exp \left(- \frac{|z|}{z_{\text{lb}}} \right) \text{Cut} \left(\frac{R - R_{\text{out}}}{\sigma_{\text{out}}} \right) \text{Cut} \left(\frac{R_{\text{in}} - R}{\sigma_{\text{in}}} \right) \quad (2.11)$$

where $C_{\perp, \text{lb}}$, x_{lb} , y_{lb} , z_{lb} , R_{out} and R_{in} are free parameters, $\sigma_{\text{out}} = \sigma_{\text{in}} = \sqrt{\frac{1}{2}}$ kpc and:

$$\text{Cut}(x) = \begin{cases} \exp(-x^2) & x > 0 \\ 1 & x \leq 0 \end{cases} \quad (2.12)$$

Note that Fujii et. al [33] did not need to include any bar components in their initial conditions as the bar components evolve naturally over the 10 Gy from their Hernquist bulge, disk and halo model initial conditions.

Finally, we have a disk with a central hole:

$$\rho_{\text{disk}}(x, y, z) \propto \exp(-R^2/2\sigma_r^2) \exp(-|z|/z_0) H(x, y) \quad (2.13)$$

where σ_r and z_0 are free parameters and for the hole we use the form adopted by Freudenreich [41]:

$$H(x, y) = 1 - \exp \left(- (R_H/O_R)^{O_N} \right) \quad (2.14)$$

with:

$$R_H^2 = (x)^2 + (\epsilon y)^2 \quad (2.15)$$

where ϵ , O_R and O_N are also free parameters. Note that Fujii et. al [33] did not have a hole in their initial disk model. This hole evolves naturally through the process of the formation of the bar over their 10 Gy simulation.

The total number of particles in our simulations are fixed. So we do not have to include the number of particles as part of our likelihood. Therefore the probability of having an N -body particle at position x, y, z will be proportional to the density of our model (ρ) at x, y, z . We have for each component of the model a parameter giving the probability a particle is from that component. We treat the probability of an N -body particle being from a component of the density distribution as parameters. These parameters, $P(\text{Disk})$, $P(\text{Bar})$, $P(\text{Hernquist})$ and $P(\text{Long Bar})$, have a Dirichlet prior [42]. This prior constrains

$$P(\text{Disk}) + P(\text{Bar}) + P(\text{Hernquist}) + P(\text{Long Bar}) = 1$$

and is uniformly distributed over any values of these parameter satisfying this condition. The log-likelihood is then:

$$\log(L) = \sum_i^N \log(\rho(x_i, y_i, z_i)) \quad (2.16)$$

where x_i , y_i and z_i are the coordinates of a particle, N is the number of particles, and ρ is the density of the model:

$$\rho(x, y, z) = P(\text{Disk})\rho_{\text{disk}}(x, y, z) + P(\text{Bar})\rho_{\text{bar}}(x, y, z) + P(\text{Hernquist})\rho_{\text{Hernquist}}(x, y, z) + P(\text{Long Bar})\rho_{\text{long bar}}(x, y, z) \quad (2.17)$$

All scale parameters are given a prior so they are uniform in $\log(\theta)$ where $\theta \in \{a_b, x_b, y_b, z_b, x_{\text{lb}}, y_{\text{lb}}, z_{\text{lb}}, \sigma_r, z_0, O_R\}$ and this implies $p(\theta) \propto 1/\theta$. In calculating the likelihood, we do not include particles for which $R > 12$ kpc or $|z| > 3$. It can be seen in Fujii et al. [33] that the scale height of the disk may start to decline between $10 \lesssim R \lesssim 15$ kpc. We also don't want the fit to be affected by particles that may have been kicked well out of the galaxy. The likelihood (L) is insensitive to being multiplied by a constant but that constant has to be the same for all parameters of our combined model. To accommodate this we normalize each density component such that

$$\int_{R \leq 12 \text{ kpc}, |z| \leq 3 \text{ kpc}} \rho_i(x, y, z) dx dy dz = 1$$

where $i \in \{\text{disk, bar, Hernquist, long bar}\}$. This integral is estimated with importance sampling. We use a set of random numbers which are transformed into the points at which we evaluate the density models in order to estimate

the normalization constant. In order to stabilize the estimation of the likelihood function these numbers are always the same every time we perform the importance sampling within a particular chain.

After running the N -body simulations, we shift the coordinates of the particles so that the center of mass is at the origin, then rotate so the bar is along the x -axis. The bar angle is estimated using the method described in Fujii et al. [33]. However, we add four parameters that we expect to be near zero to allow a further shift in the center and clockwise rotation of the model. These are α , x_{center} , y_{center} and z_{center} , with the latter three parameters in parsecs, so:

$$\begin{aligned} x_{\text{data}} &= \cos(\alpha)x + \sin(\alpha)y + x_{\text{center}}/1000 \\ y_{\text{data}} &= -\sin(\alpha)x + \cos(\alpha)y + y_{\text{center}}/1000 \\ z_{\text{data}} &= z + z_{\text{center}}/1000 \end{aligned} \tag{2.18}$$

where x_{data} , y_{data} and z_{data} are coordinates in the coordinate system of the N -body simulation. In estimating the peculiar velocity distribution scale parameter, $\hat{\sigma}_v$, above, we assumed $x \approx x_{\text{data}}$, $y \approx y_{\text{data}}$ and $z \approx z_{\text{data}}$.

To compare our model fits to the final N -body simulations we sample from the model directly, then we bin the samples. We used a simple MCMC to sample from the bar and long bar. Since the disk (excluding the hole) can be turned into an invertible cumulative distributions in R and z , and the Hernquist bulge in r , we used inverse transform sampling for those. The disk hole was handled by accepting the disk samples with probability $H(x, y)$, i.e. we used rejection sampling for the disk.

Our MCMC algorithm used to fit the models is similar to that of Foreman-Mackay et al. [43] with a mixture of the Differential Evolution [44] and snooker updates [45]. We use a simple annealing method in which we divide the log-likelihood by a temperature T which is gradually reduced to 1. This occurs during the first half of each Markov chain, which we discard. See appendix B for more details.

3 Results

In Table 1 we present the kick velocities σ_k that produce peculiar velocity distributions close to $\sigma_v = 77 \pm 6$ km s^{-1} as estimated by P20. We display the rotation curves at $t = 10$ Gyr for the three initial condition models (MWa, MWb and MWc0.8) in Fig. 1. The central values in Table 1 were used to run N -body simulations with a larger number of particles to which we fitted a parametric model. The fitted parameters are shown in Tables 2, 3 and 4. There are three potential sources of uncertainty in the model parameters: the posterior density function, variation in the likelihood between chains as a result of the importance sampling method used to estimate the normalization constant for each model component, and the possibility that Markov chains may get stuck in different local likelihood maxima. We found that for most parameters the posterior distributions overlapped significantly or, in many cases, were indistinguishable. For a few parameters we had outlier chains; these can be seen in the tables as parameters with large, highly asymmetric uncertainties. For the kicked distributions, the disk model hole parameters were very uncertain with different Markov chains settling on a wide range of different values. As this hole tended to be smaller and/or less sharp, we simply removed it, in the kicked cases, by setting $H(x, y) = 1$. We found the long bar model often acts like a second disk component when fitting to the kicked particles, this disk-like long bar was still allowed a hole through the parameter R_{in} .

We ran the N -body simulations for the two kick rate scenarios separately, but we combine the two sets of Markov chains for the ‘‘No Kick’’ columns in the parameter tables. Typically, the posterior distributions were very similar for Markov chains generated using these two sets of data, slightly expanding our 68% intervals. However, we found a difference of order 10 pc in the location of the center between simulations. For this reason, we only report the change in parameters α , x_{center} , y_{center} and z_{center} for the fits to the kicked distributions by subtracting off the median of the corresponding Markov chains. For α the fitted 68% intervals for no kick were -2° to -1° for all models, $|x_{\text{center}}|$ and $|y_{\text{center}}|$ were always $\lesssim 40$ pc, and $|z_{\text{center}}|$ was < 2 pc. We are not concerned about this difference as it is negligible compared to the bar extent.

We show the final density maps generated from the MWa initial conditions in Fig. 2. Those for MWb and MWc0.8 were similar and are given in the appendix as Figs. A.1 and A.2 respectively. These figures include both the N -body particle data as well as the fitted models. These density maps were produced by binning particles (either the N -body particles or particles drawn from the fitted model) within 0.25 kpc of the x - y , x - z and y - z planes. The density maps for the fitted models were generated by taking the average in each bin for simulated data generated

	Kick At Beginning	Uniform Kick Rate
MWa	93 ± 10	85 ± 9
MWb	97 ± 10	84 ± 10
MWc0.8	95 ± 10	84 ± 9

Table 1. Kick velocity Maxwell distribution (Eq. (2.1)) parameters (σ_k in km/s) that produce a peculiar velocity distribution where $\sigma_v = 77 \pm 6$ km/s.

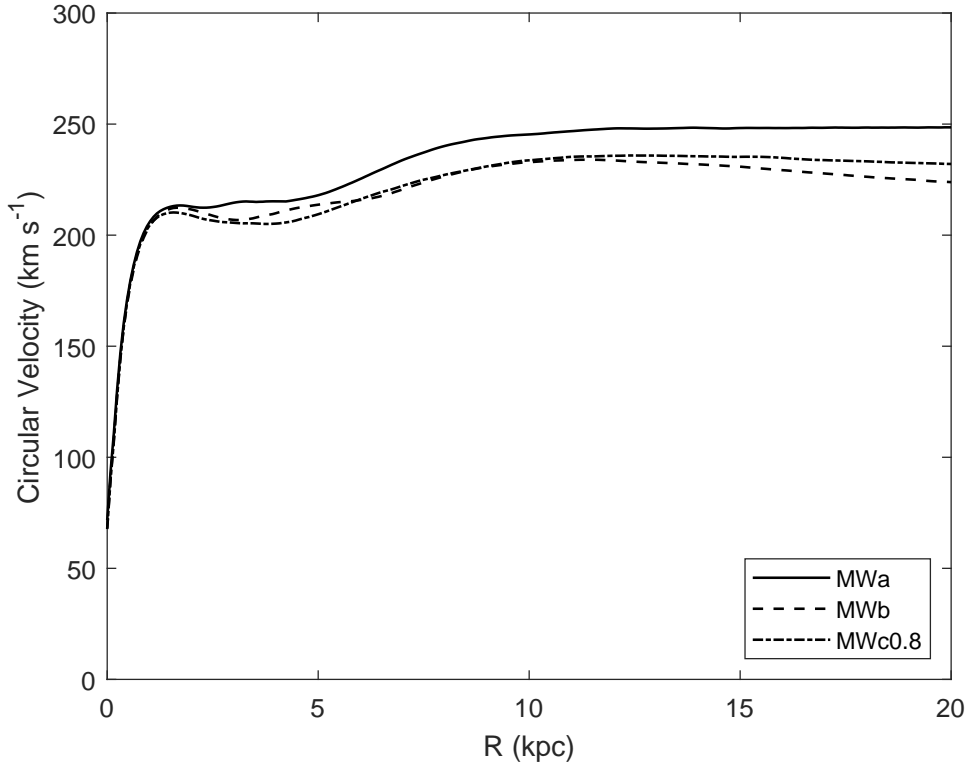


Figure 1. The rotation curves at $t = 10$ Gyr for the three initial condition models MWa, MWb and MWc0.8. They are consistent with the local circular velocity of the Sun which is measured to be 238 ± 15 km s $^{-1}$ [47]. The distance between the Sun and the Galactic Center is approximately 8 kpc.

using 500 random parameter sets from our Markov chains in each case. In Fig. 3 we show the N -body simulation data and simulated particle distributions along the x , y and z axes for the MWa case with the kicks occurring at the beginning. For the model we show the predicted mean number of particles in each bin and also the standard deviation of that prediction. This can be used to test the model fit as it provides the 68% posterior predictive intervals [46]. The corresponding uniform kick rate, MWb, and MWc0.8 cases are displayed in the appendix as Figs. A.3, A.4, A.5, A.6 and A.7. In these figures, we bin all particles within 0.25 kpc in the two perpendicular axes. We display in Fig. 4 the integrated flux along lines of sight in the central $50^\circ \times 50^\circ$ of the galaxy. The Sun is placed at a distance of 7.9 kpc, at an angle relative to the bar of 20° and at a height of 15 pc [10]. This figure was generated by binning particles in Galactic latitude and longitude with weights of $1/d^2$ where d is the distance of a particle from the Sun. We excluded particles within 1 kpc of the Sun to reduce noise. The corresponding figures for MWb and MWc0.8 are display in the appendix as Figs. A.8 and A.9 respectively.

In Table 5 we show the change in $-2\log(L)$ when replacing $\rho_{\text{bar}}(R_s)$ with a range of different models from Freudenreich [41] and Cao et al. [39]. As there is variation in the likelihood between chains, we also show the standard deviation in $-2\log(L)$. Our choice of $\rho_{\text{bar}}(R_s) \propto K_0(R_s)$ is clearly preferred over the others. The worst form, where $\rho_{\text{bar}}(R_s) \propto \exp(R_s^{-n})$, was entirely removed with $P(\text{Bar}) = 0$ and the long bar component taking over the fit in

Parameter	No Kick	Kick At Beginning	Uniform Kick Rate
$P(\text{Disk})$	$0.499^{+0.006}_{-0.005}$	$0.418^{+0.006}_{-0.006}$	$0.365^{+0.006}_{-0.004}$
$P(\text{Bar})$	$0.354^{+0.004}_{-0.005}$	$0.3220^{+0.0019}_{-0.0021}$	$0.364^{+0.005}_{-0.007}$
$P(\text{Hernquist})$	$0.0145^{+0.0013}_{-0.0018}$	$0.059^{+0.003}_{-0.002}$	$0.0647^{+0.0022}_{-0.0024}$
$P(\text{Long Bar})$	$0.1323^{+0.0025}_{-0.0025}$	$0.201^{+0.007}_{-0.007}$	$0.206^{+0.007}_{-0.010}$
σ_r (kpc)	$4.92^{+0.04}_{-0.03}$	$5.66^{+0.05}_{-0.04}$	$6.07^{+0.05}_{-0.08}$
z_0 (kpc)	$0.2238^{+0.0008}_{-0.0027}$	$1.203^{+0.023}_{-0.013}$	$1.222^{+0.018}_{-0.004}$
O_R (kpc)	$2.82^{+0.08}_{-0.11}$	—	—
O_N	$4.3^{+0.3}_{-0.2}$	—	—
ϵ	$0.780^{+0.020}_{-0.013}$	—	—
a_b (kpc)	$0.205^{+0.009}_{-0.010}$	$0.509^{+0.019}_{-0.010}$	$0.555^{+0.022}_{-0.021}$
C_\perp	$1.84^{+0.02}_{-0.05}$	$1.831^{+0.013}_{-0.015}$	$1.821^{+0.017}_{-0.015}$
C_\parallel	$3.08^{+0.11}_{-0.11}$	$2.49^{+0.03}_{-0.03}$	$2.542^{+0.019}_{-0.019}$
x_b (kpc)	$0.557^{+0.008}_{-0.008}$	$0.685^{+0.005}_{-0.005}$	$0.673^{+0.007}_{-0.011}$
y_b (kpc)	$0.367^{+0.006}_{-0.003}$	$0.455^{+0.003}_{-0.003}$	$0.445^{+0.006}_{-0.011}$
z_b (kpc)	$0.2557^{+0.0014}_{-0.0010}$	$0.3328^{+0.0014}_{-0.0015}$	$0.3155^{+0.0026}_{-0.0029}$
R_{end} (kpc)	$2.00^{+0.05}_{-0.06}$	$4.6^{+0.4}_{-0.3}$	$4.9^{+0.6}_{-0.6}$
$\Delta\alpha$ (deg)	—	$-0.34^{+0.15}_{-0.14}$	$-0.07^{+0.13}_{-0.13}$
Δx_{center} (pc)	—	$0.8^{+1.0}_{-1.1}$	$-0.7^{+1.0}_{-1.0}$
Δy_{center} (pc)	—	$-1.8^{+0.9}_{-0.9}$	$-0.3^{+0.7}_{-0.7}$
Δz_{center} (pc)	—	$-0.9^{+0.6}_{-0.5}$	$2.7^{+0.4}_{-0.5}$
x_{lb} (kpc)	5^{+5}_{-1}	$2.78^{+0.03}_{-0.03}$	$2.46^{+0.04}_{-0.03}$
y_{lb} (kpc)	$1.43^{+0.16}_{-0.07}$	$2.78^{+0.04}_{-0.04}$	$2.49^{+0.05}_{-0.04}$
z_{lb} (kpc)	$0.315^{+0.029}_{-0.010}$	$0.541^{+0.006}_{-0.011}$	$0.495^{+0.010}_{-0.014}$
$C_{\perp,\text{lb}}$	$0.88^{+0.04}_{-0.11}$	$1.764^{+0.026}_{-0.025}$	$1.983^{+0.028}_{-0.026}$
R_{out} (kpc)	$2.86^{+0.04}_{-0.05}$	$7.46^{+0.06}_{-0.04}$	$8.37^{+0.06}_{-0.06}$
R_{in} (kpc)	$1.676^{+0.018}_{-0.016}$	$2.09^{+0.03}_{-0.04}$	$2.03^{+0.07}_{-0.12}$

Table 2. Fitted parameters for model MWa. We have used the median of the MCMC chains for the central value and also included 68% confidence intervals.

the central region.

In order to estimate the kick effects on the actual Milky Way Galactic bar we used a linear fit to our simulation results of the form

$$\theta_{\text{kicked},i} = \alpha\theta_i + \beta \quad (3.1)$$

where $\theta_{\text{kicked},i}$ are the bulge parameters, x_b , y_b , and z_b for the kicked distribution and θ_i are the corresponding parameters in the non-kicked case. The α and β were found by performing a least squared fit for the values given in Tables 2, 3, and 4. We also did a similar fit for C_\perp and C_\parallel . The results are shown in Table 6 and Fig. 5. A prediction for the Milky Way bar parameters found in ref. [39] are shown in Table 7. The predicted line of sight contours for the kicked and un-kicked Milky Way bar are shown in Fig. 6.

4 Discussion and Conclusions

Our goal was to investigate the effect of neutron star birth kicks on the distribution of MSPs in the Galactic center. We began by running N -body simulations with small populations of particles kicked with a range of scales in order to estimate the required Maxwellian kick to produce a peculiar velocity distribution similar to that of resolved gamma-ray MSPs. We then reran the simulations with a larger number of particles at the required kick velocity scale and used MCMC to fit the data with a model.

We used three initial condition models intended to approximate the Milky Way, these were the MWa, MWb and MWc0.8 initial condition models of Fujii et al. [33]. Our results were consistent with theirs as can be seen, for

Parameter	No Kick	Kick At Beginning	Uniform Kick Rate
$P(\text{Disk})$	$0.506^{+0.010}_{-0.005}$	$0.6144^{+0.0024}_{-0.0026}$	$0.36^{+0.03}_{-0.04}$
$P(\text{Bar})$	$0.322^{+0.005}_{-0.003}$	$0.244^{+0.007}_{-0.003}$	$0.317^{+0.006}_{-0.003}$
$P(\text{Hernquist})$	$0.0140^{+0.0012}_{-0.0009}$	$0.0470^{+0.0022}_{-0.0021}$	$0.0819^{+0.0017}_{-0.0016}$
$P(\text{Long Bar})$	$0.154^{+0.012}_{-0.010}$	$0.094^{+0.004}_{-0.006}$	$0.24^{+0.04}_{-0.04}$
σ_r (kpc)	$5.64^{+0.06}_{-0.07}$	$5.36^{+0.03}_{-0.03}$	$6.9^{+0.7}_{-0.3}$
z_0 (kpc)	$0.2249^{+0.0003}_{-0.0003}$	$1.116^{+0.004}_{-0.014}$	$1.30^{+0.05}_{-0.06}$
O_R (kpc)	$3.19^{+0.05}_{-0.09}$	—	—
O_N	$4.25^{+0.09}_{-0.17}$	—	—
ϵ	$0.762^{+0.019}_{-0.019}$	—	—
a_b (kpc)	$0.202^{+0.004}_{-0.005}$	$0.585^{+0.023}_{-0.025}$	$0.614^{+0.014}_{-0.011}$
C_{\perp}	$2.04^{+0.08}_{-0.10}$	$2.02^{+0.03}_{-0.03}$	$1.873^{+0.016}_{-0.017}$
C_{\parallel}	$3.85^{+0.14}_{-0.08}$	$3.06^{+0.05}_{-0.05}$	$2.90^{+0.04}_{-0.04}$
x_b (kpc)	$0.548^{+0.029}_{-0.009}$	$0.587^{+0.026}_{-0.009}$	$0.710^{+0.010}_{-0.006}$
y_b (kpc)	$0.339^{+0.006}_{-0.005}$	$0.406^{+0.013}_{-0.005}$	$0.411^{+0.010}_{-0.005}$
z_b (kpc)	$0.243^{+0.004}_{-0.002}$	$0.306^{+0.007}_{-0.003}$	$0.303^{+0.004}_{-0.002}$
R_{end} (kpc)	$2.53^{+0.10}_{-0.15}$	$3.37^{+0.10}_{-0.08}$	$5.2^{+0.6}_{-0.4}$
$\Delta\alpha$ (deg)	—	$-0.04^{+0.13}_{-0.13}$	$0.30^{+0.11}_{-0.12}$
Δx_{center} (pc)	—	$4.4^{+1.2}_{-1.2}$	$2.5^{+1.2}_{-1.3}$
Δy_{center} (pc)	—	$1.8^{+0.9}_{-0.8}$	$-1.2^{+0.9}_{-0.8}$
Δz_{center} (pc)	—	$-0.6^{+0.7}_{-0.8}$	$1.4^{+0.5}_{-0.5}$
x_{lb} (kpc)	$2.7^{+0.8}_{-0.3}$	$2.1^{+0.3}_{-0.1}$	$2.78^{+0.04}_{-0.02}$
y_{lb} (kpc)	$1.14^{+0.17}_{-0.05}$	$0.93^{+0.08}_{-0.03}$	$2.65^{+0.07}_{-0.04}$
z_{lb} (kpc)	$0.414^{+0.006}_{-0.016}$	$0.656^{+0.011}_{-0.020}$	$0.56^{+0.04}_{-0.03}$
$C_{\perp,\text{lb}}$	$0.97^{+0.03}_{-0.11}$	$1.61^{+0.04}_{-0.04}$	$1.86^{+0.03}_{-0.03}$
R_{out} (kpc)	$3.66^{+0.22}_{-0.11}$	$4.67^{+0.05}_{-0.05}$	$9.32^{+0.07}_{-0.25}$
R_{in} (kpc)	$1.69^{+0.04}_{-0.03}$	$1.78^{+0.04}_{-0.03}$	$1.71^{+0.10}_{-0.06}$

Table 3. Fitted parameters for model MWb.

example, by comparing our Fig. 1 to the top left hand panels of their Figs. 1, 2, and 3 which are also consistent with the observed circular rotation velocity at the Sun’s location. In Cao et al. [39] the bar scale lengths for a modified Bessel function of the second kind model fitted to red clump giant data are 0.67, 0.29 and 0.27 for the x , y and z axes respectively, with the parameters C_{\parallel} and C_{\perp} fixed at 4 and 2. Our fits to N -body models without kicks find (x_b, y_b, z_b) of (0.56, 0.37, 0.26) for MWa, (0.55, 0.34, 0.24) for MWb and (0.55, 0.34, 0.24) for MWc0.8. We also have C_{\parallel} between 3 and 4, producing a boxy structure in x - z and y - z , this is visible in Fig. 2 for the MWa case and Figs. A.1 and A.2 for the MWb and MWc0.8 cases. The other shape parameter C_{\perp} was relatively close to 2 in all cases, resulting in a more elliptical shape in x - y . We found it was necessary to extend the bar structure using the long bar component given in Eq. 2.11. Without it the bar scale parameters would be larger, but the bar would not be long enough to explain the structure seen for $2 \text{ kpc} \lesssim |x| \lesssim 4 \text{ kpc}$ in Fig. 3 in the MWa, kicked at the beginning case, and Figs. A.3, A.4, A.5, A.6 and A.7 in the uniform kick rate, MWb and MWc0.8 cases. We find the disk scale height to be 0.22 kpc for the MWa, MWb, and MWc0.8 unknicked cases. This is at the lower end of the range of 220 to 450 pc given in Bland-Hawthorn and Gerhard [47]. There is also a small spherically symmetric Hernquist component $\sim 1\%$ of the particles in the region of interest for the unknicked cases.

Eckner et al. [31] argued using the virial theorem that kicks $\langle v^2 \rangle \lesssim (70 \text{ km s}^{-1})^2$ would lead to a “smoothing” of the distribution of 700–900 pc. We show the effect of a 400 pc and an 800 pc Gaussian smoothing on the fitted bulge (bar plus Hernquist bulge) distribution in Figs. 7 and 8 for the kicked at the beginning case. The uniform kick rate case is shown in Fig. A.10. Those figures also show the bulge component of the models with and without kicks for comparison. It is clear that a Gaussian smoothing kernel will remove the peak that survives in the N -body simulations

Parameter	No Kick	Kick At Beginning	Uniform Kick Rate
$P(\text{Disk})$	$0.555^{+0.003}_{-0.009}$	$0.467^{+0.012}_{-0.010}$	$0.357^{+0.013}_{-0.003}$
$P(\text{Bar})$	$0.318^{+0.004}_{-0.005}$	$0.262^{+0.003}_{-0.005}$	$0.305^{+0.003}_{-0.002}$
$P(\text{Hernquist})$	$0.0099^{+0.0006}_{-0.0005}$	$0.0603^{+0.0021}_{-0.0025}$	$0.0619^{+0.0019}_{-0.0020}$
$P(\text{Long Bar})$	$0.116^{+0.014}_{-0.004}$	$0.210^{+0.014}_{-0.010}$	$0.277^{+0.005}_{-0.017}$
σ_r (kpc)	$5.49^{+0.03}_{-0.04}$	$6.11^{+0.07}_{-0.09}$	$6.99^{+0.06}_{-0.19}$
z_0 (kpc)	$0.2246^{+0.0007}_{-0.0022}$	$1.266^{+0.016}_{-0.028}$	$1.262^{+0.026}_{-0.022}$
O_R (kpc)	$2.5^{+0.4}_{-0.16}$	—	—
O_N	$4.9^{+2.6}_{-1.1}$	—	—
ϵ	$0.82^{+0.12}_{-0.12}$	—	—
a_b (kpc)	$0.220^{+0.006}_{-0.006}$	$0.72^{+0.01}_{-0.04}$	$0.74^{+0.03}_{-0.03}$
C_{\perp}	$1.88^{+0.03}_{-0.03}$	$1.861^{+0.020}_{-0.020}$	$1.909^{+0.024}_{-0.022}$
C_{\parallel}	$3.37^{+0.05}_{-0.05}$	$2.69^{+0.03}_{-0.04}$	$2.69^{+0.03}_{-0.03}$
x_b (kpc)	$0.551^{+0.012}_{-0.014}$	$0.657^{+0.006}_{-0.007}$	$0.620^{+0.006}_{-0.005}$
y_b (kpc)	$0.342^{+0.007}_{-0.008}$	$0.434^{+0.005}_{-0.007}$	$0.378^{+0.005}_{-0.003}$
z_b (kpc)	$0.2395^{+0.0015}_{-0.0018}$	$0.3217^{+0.0023}_{-0.0023}$	$0.2845^{+0.0025}_{-0.0018}$
R_{end} (kpc)	$2.03^{+0.07}_{-0.10}$	$4.81^{+0.29}_{-0.25}$	$5.5^{+2.1}_{-0.9}$
$\Delta\alpha$ (deg)	—	$-0.79^{+0.18}_{-0.18}$	$0.32^{+0.13}_{-0.13}$
Δx_{center} (pc)	—	$1.4^{+1.4}_{-1.3}$	$1.0^{+1.2}_{-1.1}$
Δy_{center} (pc)	—	$-0.2^{+0.9}_{-0.9}$	$0.5^{+0.8}_{-0.8}$
Δz_{center} (pc)	—	$2.4^{+0.7}_{-0.6}$	$-0.5^{+0.5}_{-0.5}$
x_{lb} (kpc)	3^{+7}_{-1}	$2.533^{+0.023}_{-0.022}$	$2.533^{+0.020}_{-0.021}$
y_{lb} (kpc)	$1.5^{+0.4}_{-0.2}$	$2.584^{+0.027}_{-0.025}$	$2.417^{+0.021}_{-0.022}$
z_{lb} (kpc)	$0.335^{+0.006}_{-0.005}$	$0.564^{+0.019}_{-0.006}$	$0.530^{+0.010}_{-0.011}$
$C_{\perp,\text{lb}}$	$0.95^{+0.07}_{-0.11}$	$1.964^{+0.029}_{-0.029}$	$1.954^{+0.022}_{-0.022}$
R_{out} (kpc)	$3.0^{+0.1}_{-0.4}$	$7.88^{+0.07}_{-0.09}$	$9.13^{+0.13}_{-0.08}$
R_{in} (kpc)	$1.61^{+0.03}_{-0.06}$	$1.91^{+0.05}_{-0.07}$	$1.60^{+0.05}_{-0.03}$

Table 4. Fitted parameters for model MWc0.8.

$\rho_{\text{bar}}(R_s)$	Mean $-2(\Delta\log(L))$	Standard Deviation
$K_0(R_s)$	0	739
$\exp(-R_s)$	3581	1606
$\text{sech}^2(R_s)$	12795	1985
$\exp(-0.5R_s^2)$	19369	391
$(1 + R_s^n)^{-1}$	20403	953
$\exp(R_s^{-n})$	57114	3152

Table 5. Change in mean $-2\log(L)$ using different bar models $\rho_{\text{bar}}(R_s)$. The mean was taken over all the samples in the MCMC chains.

Parameter	α_i	β_i
x_b, y_b, z_b	1.13 ± 0.05	0.03 ± 0.02
C_{\perp}, C_{\parallel}	0.56 ± 0.02	0.81 ± 0.05

Table 6. Least square fit values with 68% confidence intervals for Eq. 3.1 fitted to the points shown in Figure 5.

of kicked distributions and, particularly for the 800 pc case, will produce an apparently spherically symmetric bulge.

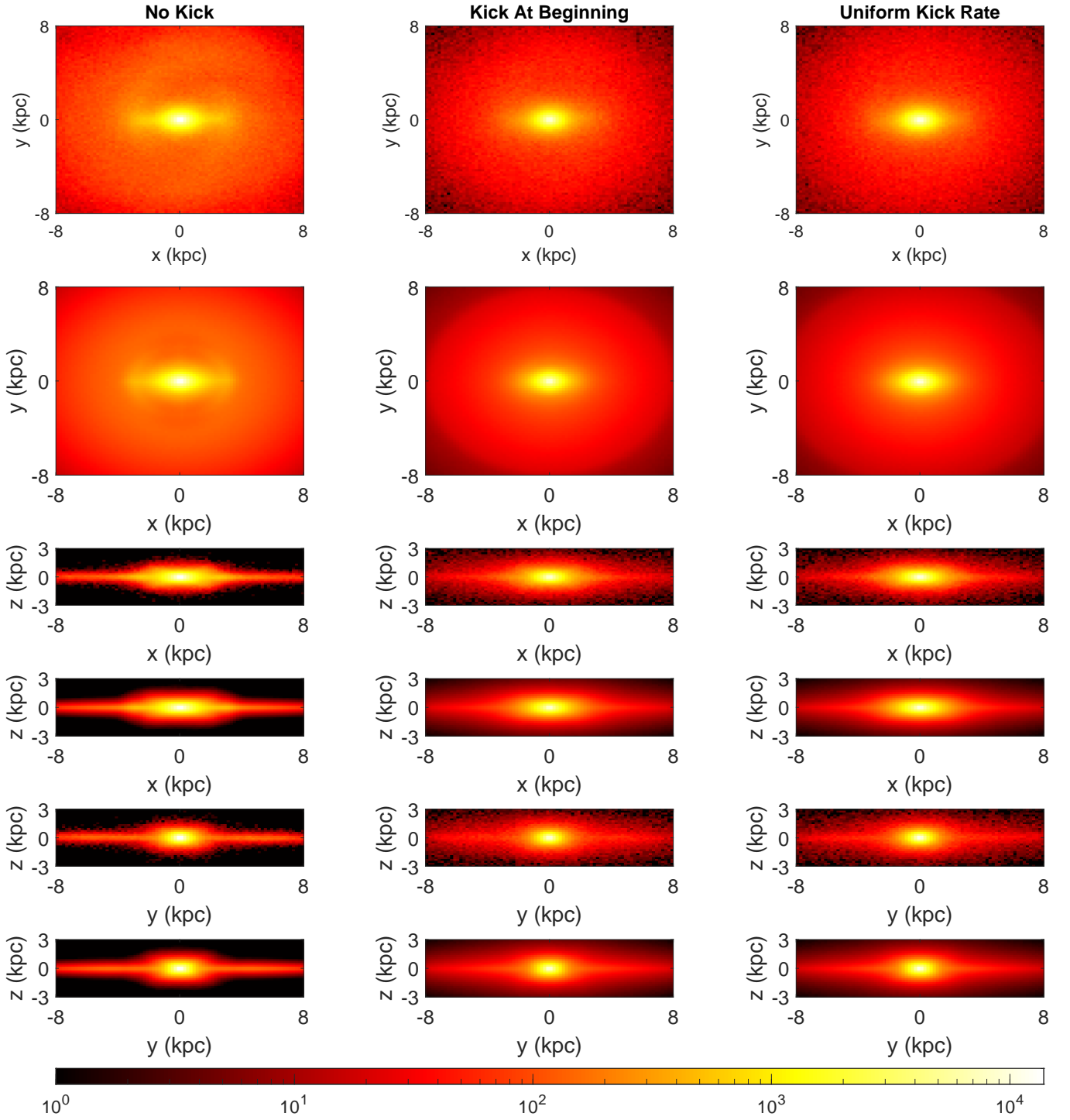


Figure 2. Final density map of particles with no kick, a kick at the beginning and a uniform kick rate generated from the MWa initial conditions. Every second row shows the fitted model.

Parameter	x_b (kpc)	y_b (kpc)	z_b (kpc)	C_{\perp}	C_{\parallel}
Not kicked	0.67	0.29	0.27	2	4
Kicked	0.79 ± 0.02	0.36 ± 0.01	0.35 ± 0.01	1.93 ± 0.02	3.05 ± 0.03

Table 7. Predictions with 68% confidence intervals for the kicked spatial distribution for the Milky Way bar model found in ref. [39] using Eq. 3.1 and the parameter values given in Table 6.

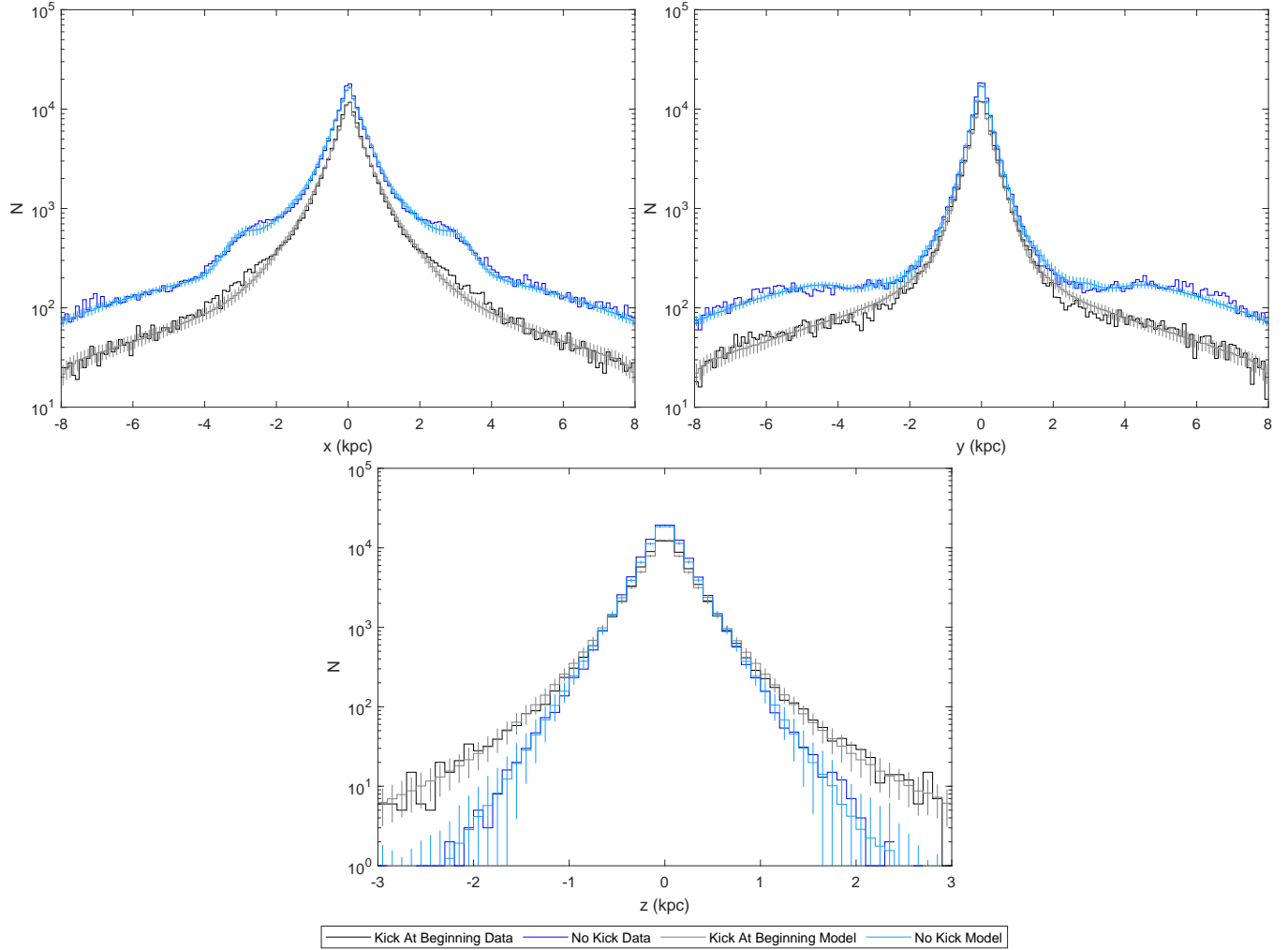


Figure 3. Profile along x , y and z axes with kicks occurring at the beginning for the case generated from the MWa initial conditions. We show both the final N -body simulation data and data simulated using the final fitted model. For the final fitted model we show the mean number of particles in each bin and the standard deviation.

From the peculiar velocity data we inferred kicks that are larger than assumed by Eckner et al. [31] with σ_k at around $80\text{--}100 \text{ km s}^{-1}$ ($\langle v^2 \rangle = 3\sigma_k^2$ for a Maxwell distribution where the angular brackets signify the mean value) so the smoothing effect of the Gaussian would be even more severe. We show an even smaller Gaussian smoothing of 200 pc in Figs. 9 and 10 for the kicked at beginning case and in Fig. A.11 for the uniform kick rate case. We also show in Fig. 11 the profile for particles with smaller kick scales between 0 km s^{-1} and 80 km s^{-1} for the kicked at the beginning case. The corresponding uniform kick rate case is shown in Fig. A.12. In these two figures, each kick scale has only 4×10^5 particles; therefore, to reduce noise, the bins in each of the other two dimensions are twice as big as in previous single dimensional plots, and particles within 0.5 kpc (previously 0.25 kpc) of the axis are included. The profiles along the z axis in particular show that there is a reduction in the slope as the kick velocities increase, along the other two axes the general increase in scaleheight is seen as a reduction in density. These results demonstrates that Gaussian smoothing is not a good way of modelling a kicked version of a boxy bulge/bar template.

In every case, the bar fitted to the kicked data is both broader, with larger scale parameters x_b , y_b and z_b , and less boxy, with smaller C_{\parallel} . For example, for the MWa initial conditions (x_b, y_b, z_b) increases from $(0.56, 0.37, 0.26)$ to $(0.69, 0.46, 0.33)$ and $(0.67, 0.45, 0.32)$ for the kick at beginning case and the uniform kick rate case respectively, while C_{\parallel} declines from 3.08 to 2.49 and 2.54. The spherically symmetric Hernquist bulge increases from $\sim 1\%$ of the particles to 6% for MWa. Like the bar, it becomes broader with a_b increasing from around 0.2 kpc to 0.51 kpc and 0.56 kpc. For the other two models similar changes occur, $P(\text{Long Bar})$ and a_b both increase significantly. In MSP model A1 of P20, the disk parameters were $\sigma_r = 4.5^{+0.5}_{-0.4} \text{ kpc}$ and $z_0 = 0.71^{+0.11}_{-0.09}$. In the current article, after

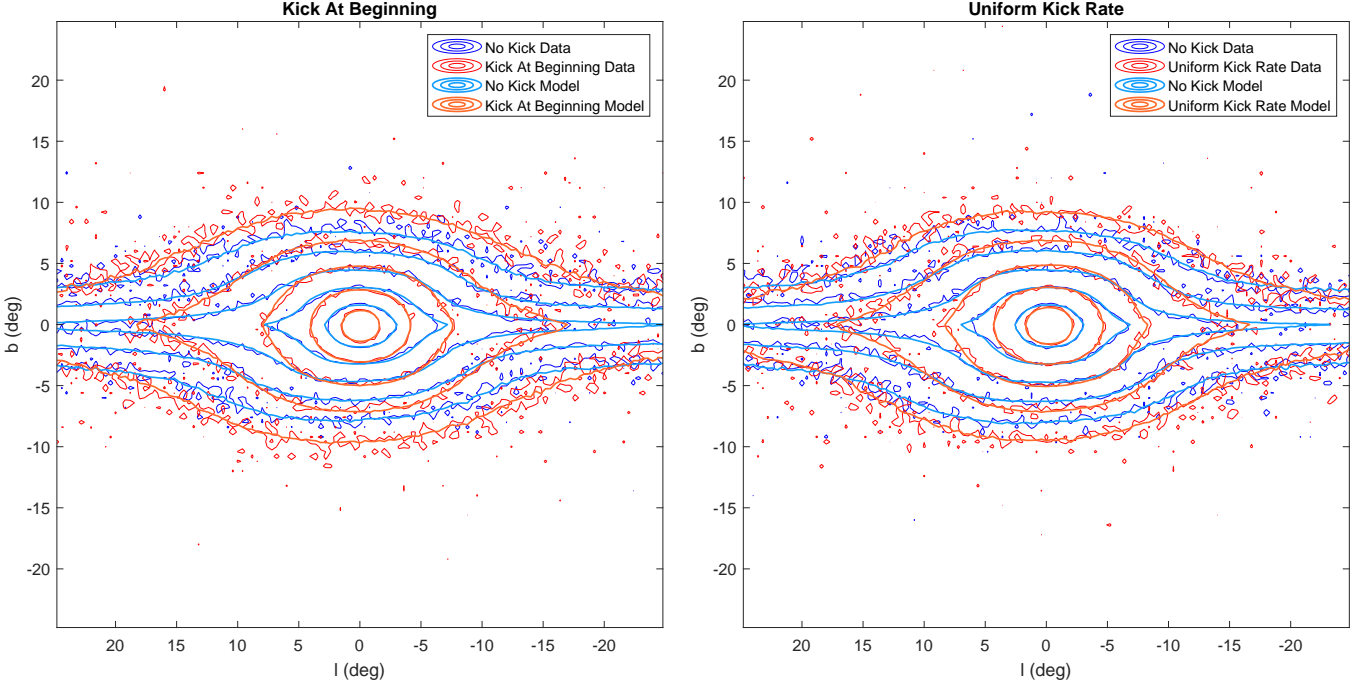


Figure 4. Final flux distribution in Galactic coordinates generated from the MWA initial conditions. The contours for each distribution are at 1, 2, 4, 8 and 16 times the mean in this region. The Sun is placed at a distance of 7.9 kpc, at an angle relative to the bar of 20° and at a height of 15 pc.

being kicked, the disk scale heights z_0 of all models increase from 0.22 kpc to $\gtrsim 1$ kpc, while σ_r is in the range 5–7 kpc. However, we find that in all kicked cases, except for MWb with kicks occurring at the beginning, the long bar behaves like a relatively thin disk component. We have $x_{\text{lb}} \approx y_{\text{lb}}$, $C_{\perp, \text{lb}} \sim 2$ and $R_{\text{out}} \gtrsim 7$, resulting in a density $\sim \exp(-R/R_0)$ in R for scalelength R_0 . These scalelengths would then be between approximately 2.4 kpc and 2.8 kpc. For comparison, in Bland-Hawthorn and Gerhard [47] the Milky Way disk scalelength is reported as 2.6 ± 0.5 kpc. The exponential scaleheights of these “long bars” range between about 0.5–0.6 kpc. In Fig. 3, for the MWA kicked at the beginning case and in Figs. A.3, A.5, A.6 and A.7 for the uniform kick rate and MWb, and MWc0.8 case, there may be, to varying degrees, an excess of kicked particles over the model in the region of $2 \text{ kpc} \lesssim |x| \lesssim 4 \text{ kpc}$. This can be seen as a correlated run of roughly two standard deviation difference between the prediction and the data in this region.

Although, a more complicated parametric model could remedy these fit defects, our main aim in this article was to estimate the effect of the MSP kicks on their distribution in the Milky Way Galactic bar. As can be seen for the MWA case from Fig. 4, the line of sight integral of the models are a good match to the simulations. In particular the noisy simulation contours scatter in an unbiased way around the smooth model contours. Similar results can be seen for the MWb and MWc0.8 cases in Figs. A.8 and A.9 respectively.

We used the same bar parametric model as Cao et al. [39] who fit the best fit parameters to the red clump luminosity density distribution of the Galactic bar measured by the Optical Gravitational Lensing Experiment (OGLE) III survey. Comparing to their fit, our final simulation fits of the unkicked particles had somewhat different bulge parameters. But, there appears to be a linear relationship between the unkicked scale parameters x_b , y_b , and z_b and their kicked counterparts. Similarly, there appears to be a linear relationship between C_{\perp} , C_{\parallel} , and their kicked counterparts. Therefore, we were able to estimate the Milky Way Galactic bar kicked parameters as shown in Fig. 5 and Table 7. The residuals in this least squares fit are partially due to the systematic error of our model misfit and also the Cao et al. [39] model misfit to the red clump data. As can be seen, there is more scatter in the x_b parameter. This is not unexpected due to the already mentioned degeneracy with the long bar. Also, as can be seen, estimating the Milky Way bar kicked x_b parameter did involve a reasonable amount of extrapolation and so future simulations which have a larger x_b will be needed to check it. A made-to-measure [48, 49] approach may be needed. This would also be advantageous as it could take into account the X/peanut shaped morphology of the bar [40, 50, 51] as done in

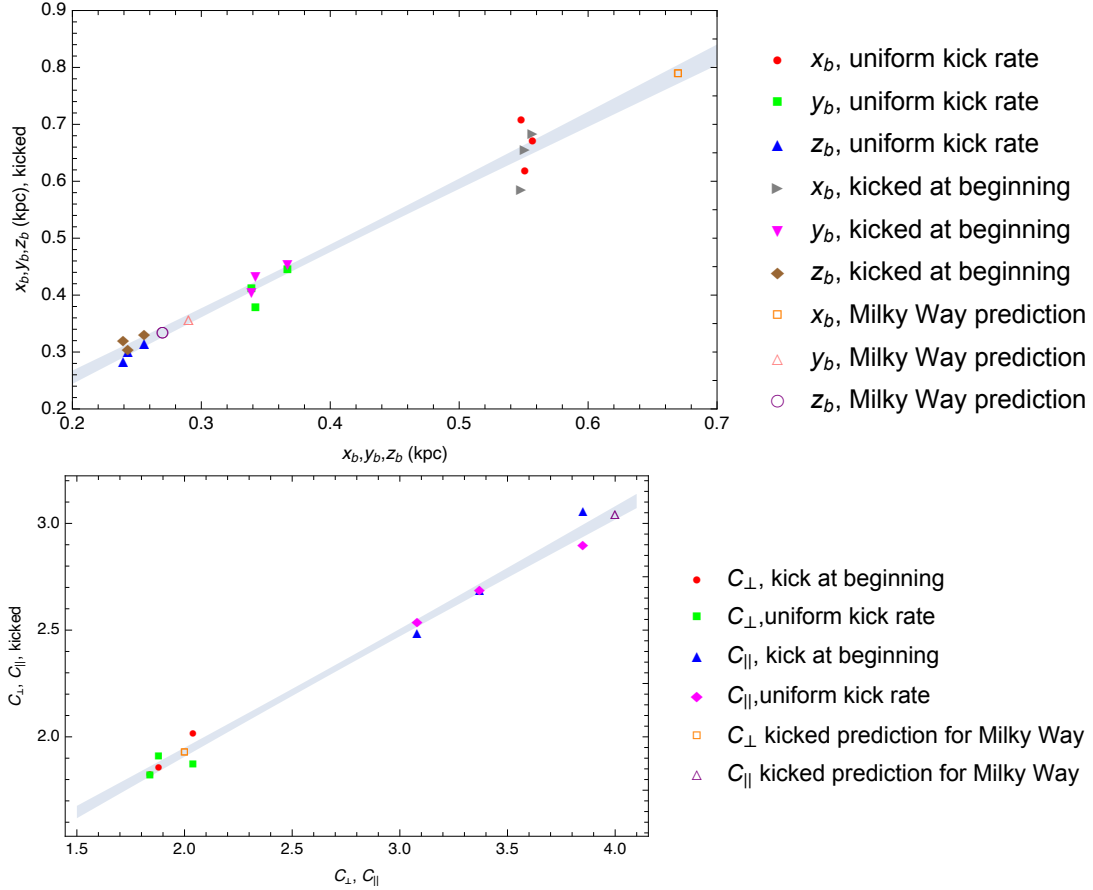


Figure 5. Simulation parameters with 68% confidence interval bands for straight line model fits. The closed symbol values are obtained from values given in Tables 2, 3, and 4. The predictions for the ref. [39] model of the Milky Way Galaxy are given as open symbols.

ref. [52]. There is some preliminary evidence that the X-shape may improve the fit to the Fermi-LAT gamma-ray data [10].

In conclusion, we used N -body simulations to explore the effect of a Maxwell distributed kick on the distribution of MSPs in the Galactic center. We find that while a 700–900 pc Gaussian smoothing of the stellar mass would be too aggressive, the bulge distribution of the kicked particles is slightly broader and less boxy. From these results, we expect the GCE to deviate by a small amount from the stellar mass spatial distribution in the Galactic center. Also, as can be seen from Table 7, we would not expect the GCE to appear spherically symmetric due to the MSP kicks as that would require $x_b = y_b = z_b$ and $C_{\perp} = C_{\parallel} = 2$ which are far from our inferred points relative to their error bars.

The amount of spatial smoothing of the bulge MSPs will depend on the proportion of MSPs in the bulge that are made from the recycling channel and the proportion that are made from the accretion induced collapse channel. Motivated by similarities between the bulge and disk population seen by P20 we have assumed this mixture has the same proportions as the disk MSPs. If the GCE is due to bulge MSPs, its morphology could be used to check our smoothing prediction by comparing if there are any deviations between the GCE morphology and the stellar spatial distribution. A complication to this approach would be the possibility of some smearing of the GCE due to cosmic ray electron diffusion [53, 54]. An additional complication is that if the MSP is spun up by a captured star then the MSP spatial distribution would be proportional to the stellar density squared [8, 31]. We have been assuming that the MSPs formed in a binary system and so have a spatial distribution proportional to the stellar density. Eventually, once the bulge MSPs are resolved [30, 55], comparing their spatial distribution to the stellar distribution should provide independent information to more robustly estimate the natal kick distribution.

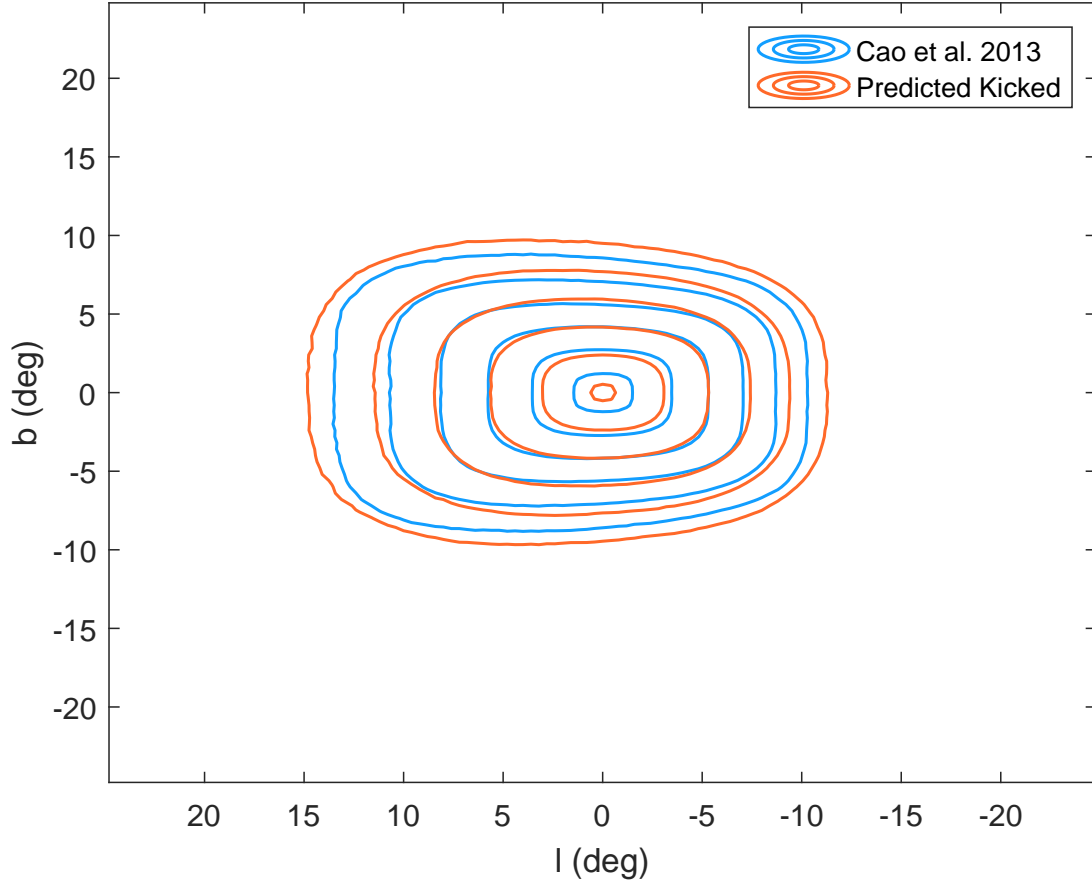


Figure 6. Line of sight contours for model of the Milky Way bar given by Cao et al. [39]. Both the model and its kicked version, obtained from the parameters in Table 7, are shown. As in ref. [39] the Galactic Centre is taken to be 8.13 kpc away and the angle of the bulge to be 29° . Contours are from 1 to 32 times the mean of the corresponding case given in steps of factors of 2.

Acknowledgments

We thank Roland Crocker and Oscar Macias for helpful comments. HP was supported by a University of Canterbury Doctoral Scholarship.

References

- [1] L. Goodenough and D. Hooper, *Possible Evidence For Dark Matter Annihilation In The Inner Milky Way From The Fermi Gamma Ray Space Telescope*, *arXiv e-prints* (Oct., 2009) arXiv:0910.2998, [0910.2998].
- [2] D. Hooper and T. Linden, *Origin of the gamma rays from the galactic center*, *Physical Review D* **84** (Dec, 2011) .
- [3] K. N. Abazajian and M. Kaplinghat, *Detection of a Gamma-Ray Source in the Galactic Center Consistent with Extended Emission from Dark Matter Annihilation and Concentrated Astrophysical Emission*, *Phys. Rev.* **D86** (2012) 083511, [1207.6047].
- [4] C. Gordon and O. Macias, *Dark Matter and Pulsar Model Constraints from Galactic Center Fermi-LAT Gamma Ray Observations*, *Phys. Rev.* **D88** (2013) 083521, [1306.5725].
- [5] K. N. Abazajian, *The Consistency of Fermi-LAT Observations of the Galactic Center with a Millisecond Pulsar Population in the Central Stellar Cluster*, *JCAP* **1103** (2011) 010, [1011.4275].
- [6] O. Macias, C. Gordon, R. M. Crocker, B. Coleman, D. Paterson, S. Horiuchi et al., *Galactic bulge preferred over dark matter for the galactic centre gamma-ray excess*, *Nature Astronomy* **2** (Mar, 2018) 387–392.
- [7] R. Bartels, E. Storm, C. Weniger and F. Calore, *The Fermi-LAT GeV excess as a tracer of stellar mass in the Galactic bulge*, *Nature Astronomy* (Aug., 2018) , [1711.04778].

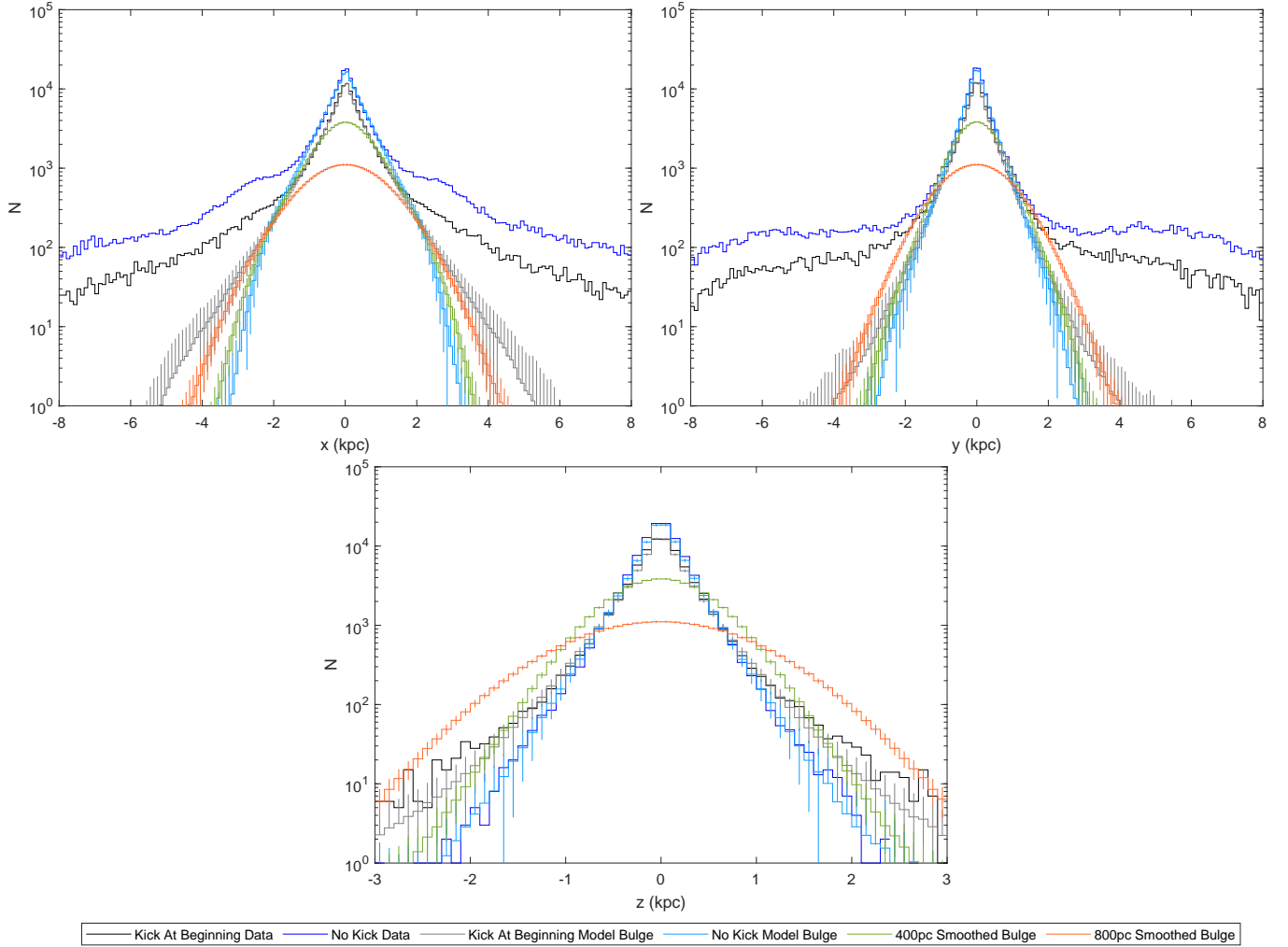


Figure 7. Final profile along x , y and z axes with kicks occurring at the beginning generated from the MWa initial conditions. Here we show the fitted bulge components, which consist of the bar plus Hernquist bulge, as well as the no kick bulge smoothed with 400 pc and 800 pc Gaussians. We show both N -body simulation data and data simulated using the fitted model. For the fitted model we show the mean number of particles in each bin and the standard deviation.

- [8] O. Macias, S. Horiuchi, M. Kaplinghat, C. Gordon, R. M. Crocker and D. M. Nataf, *Strong evidence that the galactic bulge is shining in gamma rays*, *JCAP* **2019** (Sept., 2019) 042, [[1901.03822](#)].
- [9] K. N. Abazajian, S. Horiuchi, M. Kaplinghat, R. E. Keeley and O. Macias, *Strong constraints on thermal relic dark matter from Fermi-LAT observations of the Galactic Center*, *Phys. Rev. D* **102** (2020) 043012, [[2003.10416](#)].
- [10] B. Coleman, D. Paterson, C. Gordon, O. Macias and H. Ploeg, *Maximum entropy estimation of the Galactic bulge morphology via the VVV Red Clump*, *MNRAS* **495** (May, 2020) 3350–3372, [[1911.04714](#)].
- [11] F. Calore, F. Donato and S. Manconi, *Dissecting the inner Galaxy with γ -ray pixel count statistics*, *arXiv e-prints* (Feb., 2021) arXiv:2102.12497, [[2102.12497](#)].
- [12] M. Di Mauro, *Characteristics of the Galactic Center excess measured with 11 years of Fermi-LAT data*, *Phys. Rev. D* **103** (Mar., 2021) 063029, [[2101.04694](#)].
- [13] R. Bartels, S. Krishnamurthy and C. Weniger, *Strong support for the millisecond pulsar origin of the Galactic center GeV excess*, *Phys. Rev. Lett.* **116** (2016) 051102, [[1506.05104](#)].
- [14] S. K. Lee, M. Lisanti, B. R. Safdi, T. R. Slatyer and W. Xue, *Evidence for Unresolved γ -Ray Point Sources in the Inner Galaxy*, *Phys. Rev. Lett.* **116** (2016) 051103, [[1506.05124](#)].
- [15] R. K. Leane and T. R. Slatyer, *Dark Matter Strikes Back at the Galactic Center*, *arXiv e-prints* (Apr., 2019) arXiv:1904.08430, [[1904.08430](#)].

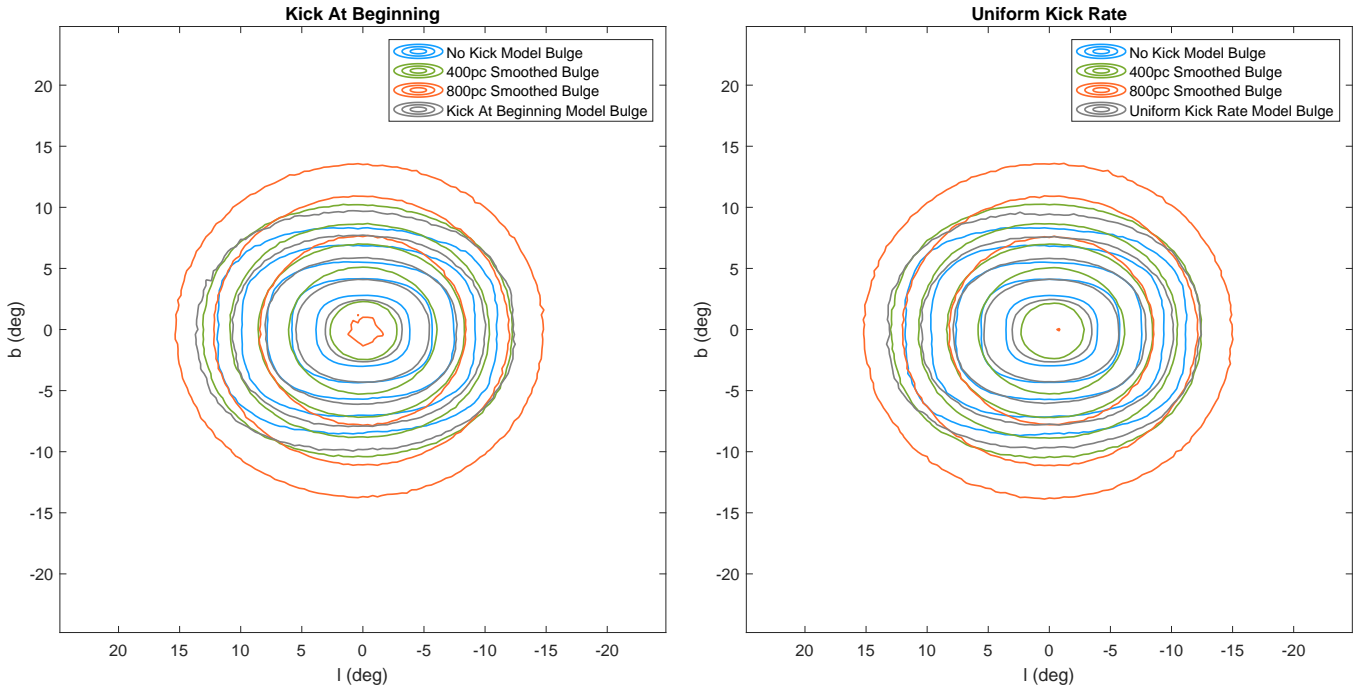


Figure 8. Final bulge, consisting of bar plus Hernquist bulge, flux distribution in Galactic coordinates generated from the MWA initial conditions. We also show the no kick bulge smoothed with 400 pc and 800 pc Gaussians. The contours for each distribution are at 1, 2, 4, 8 and 16 times the mean in this region. The Sun is placed at a distance of 7.9 kpc, at an angle relative to the bar of 20° and at a height of 15 pc.

- [16] R. K. Leane and T. R. Slatyer, *The enigmatic Galactic Center excess: Spurious point sources and signal mismodeling*, *Phys. Rev. D* **102** (Sept., 2020) 063019, [2002.12371].
- [17] R. K. Leane and T. R. Slatyer, *Spurious Point Source Signals in the Galactic Center Excess*, *Phys. Rev. Lett.*, **125** (Sept., 2020) 121105, [2002.12370].
- [18] M. Buschmann, N. L. Rodd, B. R. Safdi, L. J. Chang, S. Mishra-Sharma, M. Lisanti et al., *Foreground mismodeling and the point source explanation of the Fermi Galactic Center excess*, *Phys. Rev. D* **102** (July, 2020) 023023, [2002.12373].
- [19] L. J. Chang, S. Mishra-Sharma, M. Lisanti, M. Buschmann, N. L. Rodd and B. R. Safdi, *Characterizing the nature of the unresolved point sources in the Galactic Center: An assessment of systematic uncertainties*, *Phys. Rev. D* **101** (Jan., 2020) 023014, [1908.10874].
- [20] D. Bhattacharya and E. P. J. van den Heuvel, *Formation and evolution of binary and millisecond radio pulsars*, *Physics Reports* **203** (Jan., 1991) 1–124.
- [21] L. Ferrario and D. Wickramasinghe, *The birth properties of Galactic millisecond radio pulsars*, *Mon. Not. Roy. Astron. Soc.* **375** (01, 2007) 1009–1016.
- [22] J. R. Hurley, C. A. Tout, D. T. Wickramasinghe, L. Ferrario and P. D. Kiel, *Formation of binary millisecond pulsars by accretion-induced collapse of white dwarfs*, *Mon. Not. Roy. Astron. Soc.* **402** (02, 2010) 1437–1448.
- [23] A. J. Ruiter, L. Ferrario, K. Belczynski, I. R. Seitenzahl, R. M. Crocker and A. I. Karakas, *On the formation of neutron stars via accretion-induced collapse in binaries*, *Mon. Not. Roy. Astron. Soc.* **484** (Mar., 2019) 698–711, [1802.02437].
- [24] A. Gautam, R. M. Crocker, L. Ferrario, A. J. Ruiter, H. Ploeg, C. Gordon et al., *Millisecond Pulsars from Accretion Induced Collapse naturally explain the Galactic Center Gamma-ray Excess*, *arXiv e-prints* (June, 2021) arXiv:2106.00222, [2106.00222].
- [25] C. Fryer, W. Benz, M. Herant and S. A. Colgate, *What can the accretion-induced collapse of white dwarfs really explain?*, *Astrophys. J.* **516** (may, 1999) 892–899.
- [26] F. S. Kitaura, H.-T. Janka and W. Hillebrandt, *Explosions of o-ne-mg cores, the crab supernova, and subluminescent type ii-p supernovae*, *Astronomy & Astrophysics* **450** (Apr, 2006) 345–350.
- [27] A. G. Lyne and D. R. Lorimer, *High birth velocities of radio pulsars*, *Nature* **369** (May, 1994) 127–129.

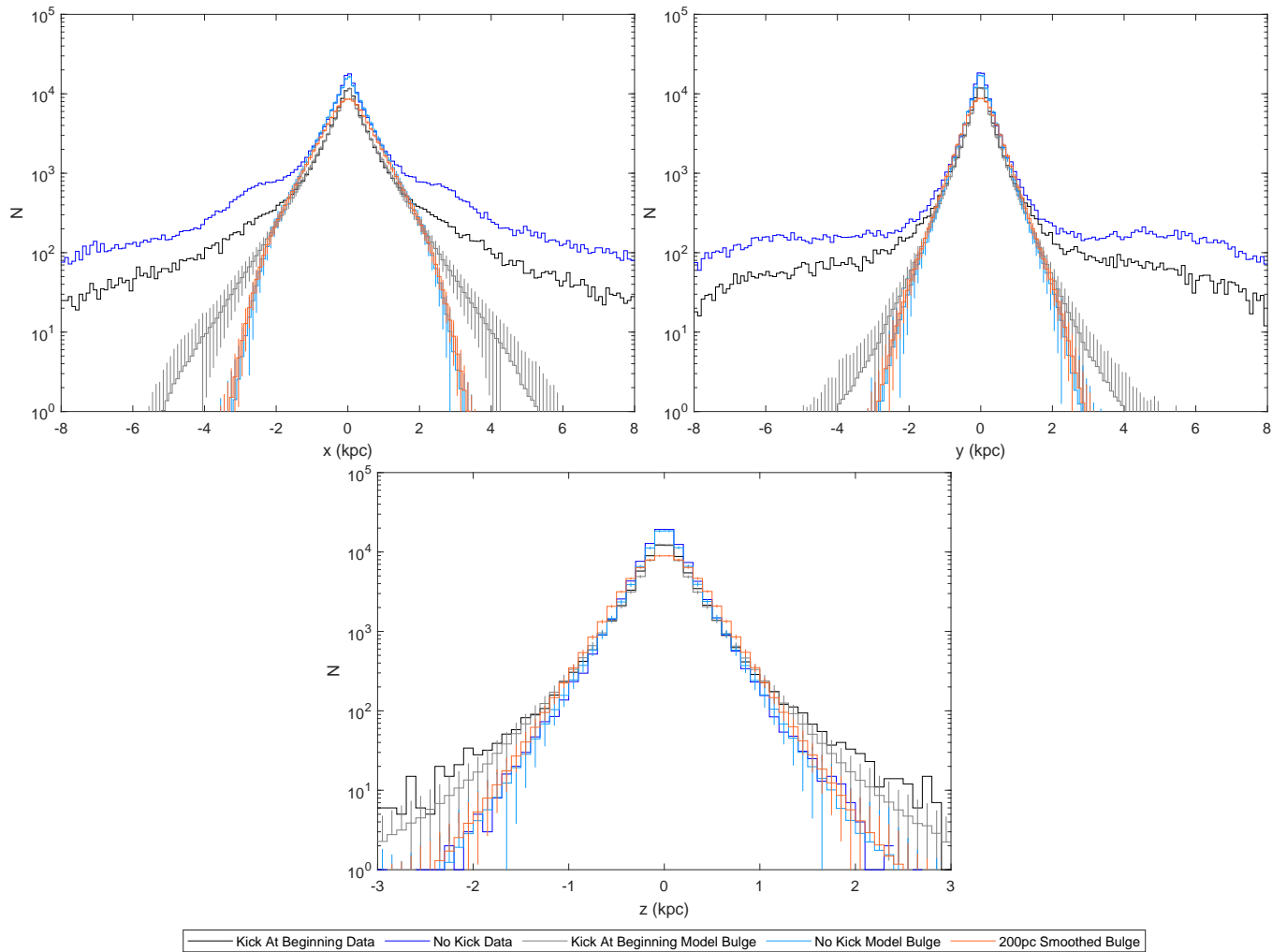


Figure 9. Final profile along x , y and z axes with kicks occurring at the beginning generated from the MWa initial conditions. Here we show the fitted bulge components as well as the no kick bulge smoothed with a 200 pc Gaussian. We show both N -body simulation data and data simulated using the fitted model. For the fitted model we show the mean number of particles in each bin and the standard deviation.

- [28] Wongwathanarat, A., Janka, H.-Th. and Müller, E., *Three-dimensional neutrino-driven supernovae: Neutron star kicks, spins, and asymmetric ejection of nucleosynthesis products*, *Astron. and Astrophys.* **552** (2013) A126.
- [29] E. Bear and N. Soker, *Neutron star natal kick and jets in core collapse supernovae*, *Astrophys. J.* **855** (mar, 2018) 82.
- [30] H. Ploeg, C. Gordon, R. Crocker and O. Macias, *Comparing the galactic bulge and galactic disk millisecond pulsars*, *JCAP* **2020** (Dec., 2020) 035, [2008.10821].
- [31] C. Eckner, X. Hou, P. D. Serpico, M. Winter, G. Zaharijas, P. Martin et al., *Millisecond Pulsar Origin of the Galactic Center Excess and Extended Gamma-Ray Emission from Andromeda: A Closer Look*, *ApJ* **862** (July, 2018) 79, [1711.05127].
- [32] J. Bédorf, E. Gaburov and S. Portegies Zwart, *A sparse octree gravitational N -body code that runs entirely on the GPU processor*, *Journal of Computational Physics* **231** (Apr., 2012) 2825–2839, [1106.1900].
- [33] M. S. Fujii, J. Bédorf, J. Baba and S. Portegies Zwart, *Modelling the Milky Way as a dry Galaxy*, *MNRAS* **482** (Jan., 2019) 1983–2015, [1807.10019].
- [34] K. Kuijken and J. Dubinski, *Nearly Self-Consistent Disc / Bulge / Halo Models for Galaxies*, *MNRAS* **277** (Dec., 1995) 1341.
- [35] L. M. Widrow and J. Dubinski, *Equilibrium Disk-Bulge-Halo Models for the Milky Way and Andromeda Galaxies*, *ApJ* **631** (Oct., 2005) 838–855, [astro-ph/0506177].

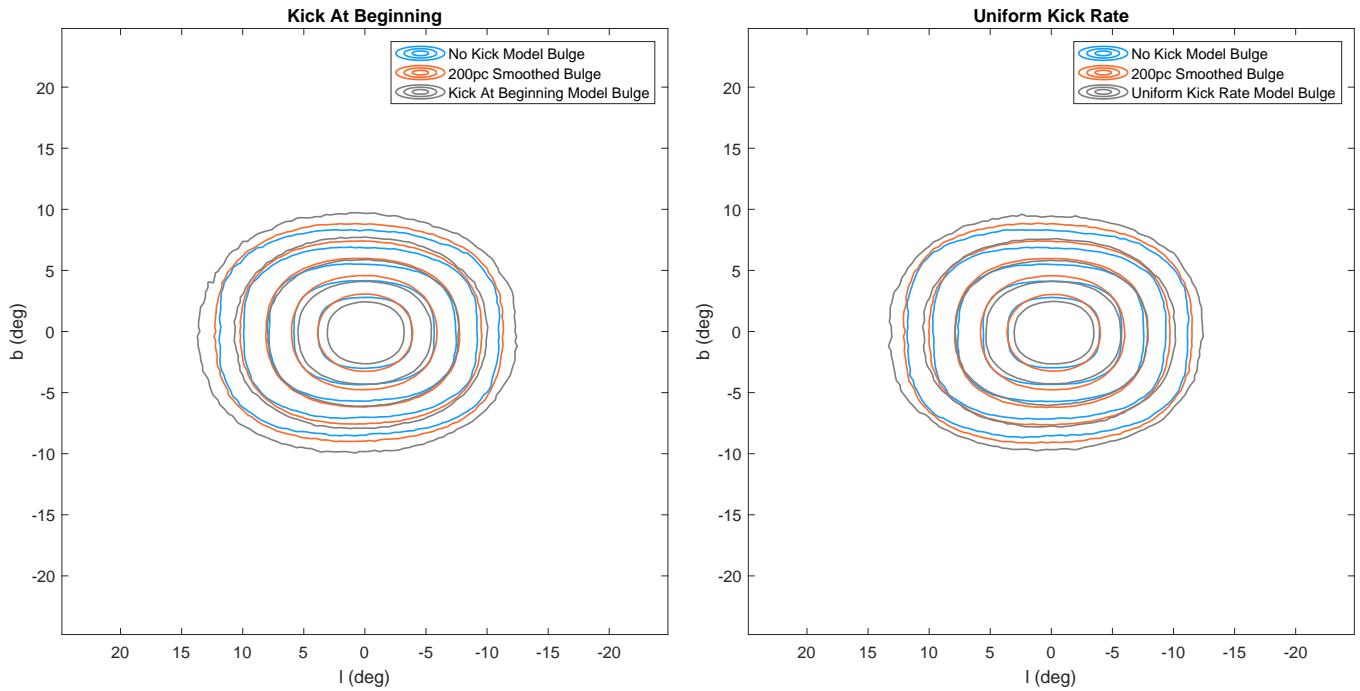


Figure 10. Final bulge flux distribution in Galactic coordinates generated from the MWa initial conditions. We also show the no kick bulge smoothed with a 200 pc Gaussian. The contours for each distribution are at 1, 2, 4, 8 and 16 times the mean in this region. The Sun is placed at a distance of 7.9 kpc, at an angle relative to the bar of 20° and at a height of 15 pc.

- [36] L. M. Widrow, B. Pym and J. Dubinski, *Dynamical Blueprints for Galaxies*, *ApJ* **679** (June, 2008) 1239–1259, [0801.3414].
- [37] F. Verbunt, A. Igoshev and E. Cator, *The observed velocity distribution of young pulsars*, *A&A* **608** (Dec., 2017) A57, [1708.08281].
- [38] L. Hernquist, *An Analytical Model for Spherical Galaxies and Bulges*, *ApJ* **356** (June, 1990) 359.
- [39] L. Cao, S. Mao, D. Nataf, N. J. Rattenbury and A. Gould, *A New Photometric Model of the Galactic Bar using Red Clump Giants*, *Mon. Not. Roy. Astron. Soc.* **434** (2013) 595–605, [1303.6430].
- [40] C. Wegg, O. Gerhard and M. Portail, *The structure of the Milky Way’s bar outside the bulge*, *MNRAS* **450** (July, 2015) 4050–4069, [1504.01401].
- [41] H. T. Freudenreich, *A COBE Model of the Galactic Bar and Disk*, *ApJ* **492** (Jan., 1998) 495–510, [astro-ph/9707340].
- [42] M. Betancourt, *Cruising the simplex: Hamiltonian Monte Carlo and the Dirichlet distribution*, in *American Institute of Physics Conference Series* (P. Goyal, A. Giffin, K. H. Knuth and E. Vrscay, eds.), vol. 1443 of *American Institute of Physics Conference Series*, pp. 157–164, May, 2012. 1010.3436. DOI.
- [43] D. Foreman-Mackey, D. W. Hogg, D. Lang and J. Goodman, *emcee: The MCMC Hammer*, *Publications of the Astronomical Society of the Pacific* **125** (Mar., 2013) 306, [1202.3665].
- [44] C. ter Braak, *A markov chain monte carlo version of the genetic algorithm differential evolution: Easy bayesian computing for real parameter spaces*, *Statistics and Computing* **16** (09, 2006) 239–249.
- [45] C. ter Braak and J. Vrugt, *Differential evolution markov chain with snooker updater and fewer chains*, *Statistics and Computing* **18** (12, 2008) 435–446.
- [46] A. Gelman, J. B. Carlin, H. S. Stern, D. B. Dunson, A. Vehtari and D. B. Rubin, *Bayesian Data Analysis*. CRC Press, 3 ed., 2013.
- [47] J. Bland-Hawthorn and O. Gerhard, *The Galaxy in Context: Structural, Kinematic, and Integrated Properties*, *Annual Review of Astronomy and Astrophysics* **54** (Sept., 2016) 529–596, [1602.07702].
- [48] D. Syer and S. Tremaine, *Made-to-measure N-body systems*, *MNRAS* **282** (Sept., 1996) 223–233, [astro-ph/9605061].

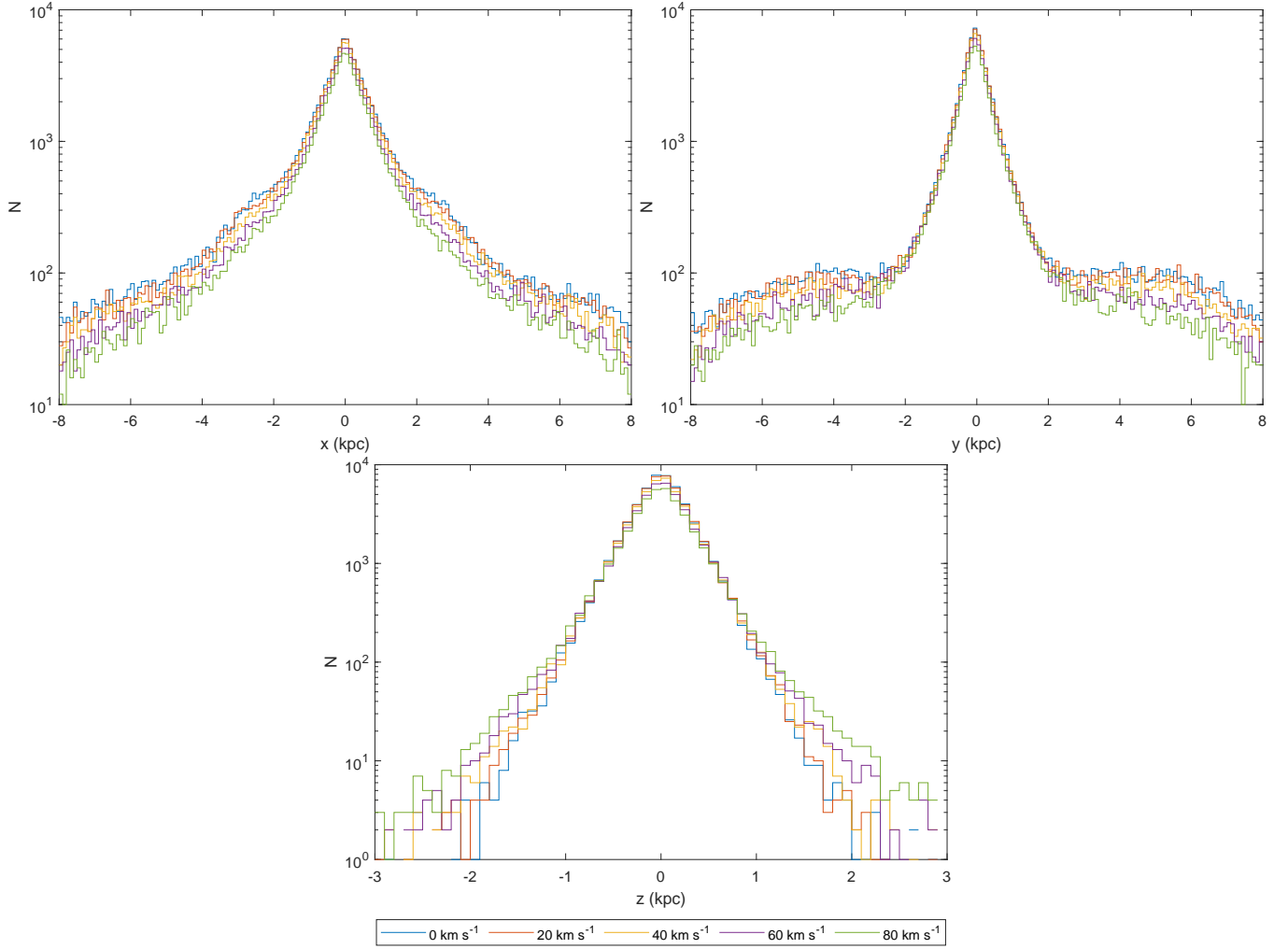


Figure 11. Final profile along x , y and z axes with kicks occurring at the beginning for kicks between 0 km s^{-1} and 80 km s^{-1} in 20 km s^{-1} increments. Generated from the MWA initial conditions.

- [49] F. de Lorenzi, V. P. Debattista, O. Gerhard and N. Sambhus, *NMAGIC: a fast parallel implementation of a χ^2 -made-to-measure algorithm for modelling observational data*, *MNRAS* **376** (Mar., 2007) 71–88, [[astro-ph/0701582](#)].
- [50] D. M. Nataf, A. Udalski, A. Gould, P. Fouqué and K. Z. Stanek, *The Split Red Clump of the Galactic Bulge from OGLE-III*, *Astrophys. J. lett.* **721** (Sept., 2010) L28–L32, [[1007.5065](#)].
- [51] A. McWilliam and M. Zoccali, *Two Red Clumps and the X-shaped Milky Way Bulge*, *ApJ* **724** (Dec., 2010) 1491–1502, [[1008.0519](#)].
- [52] M. Portail, C. Wegg, O. Gerhard and I. Martinez-Valpuesta, *Made-to-measure models of the Galactic box/peanut bulge: stellar and total mass in the bulge region*, *MNRAS* **448** (Mar., 2015) 713–731, [[1502.00633](#)].
- [53] D. Song, O. Macias and S. Horiuchi, *Inverse Compton emission from millisecond pulsars in the Galactic bulge*, *Phys. Rev. D* **99** (June, 2019) 123020, [[1901.07025](#)].
- [54] O. Macias, H. van Leijen, D. Song, S. Ando, S. Horiuchi and R. M. Crocker, *Cherenkov telescope array sensitivity to the putative millisecond pulsar population responsible for the galactic center excess*, *Monthly Notices of the Royal Astronomical Society* (May, 2021).
- [55] F. Calore, M. Di Mauro, F. Donato, J. W. T. Hessels and C. Weniger, *Radio Detection Prospects for a Bulge Population of Millisecond Pulsars as Suggested by Fermi-LAT Observations of the Inner Galaxy*, *ApJ* **827** (Aug., 2016) 143, [[1512.06825](#)].
- [56] H. Haario, E. Saksman and J. Tamminen, *An adaptive metropolis algorithm*, *Bernoulli* **7** (2001) 223–242.

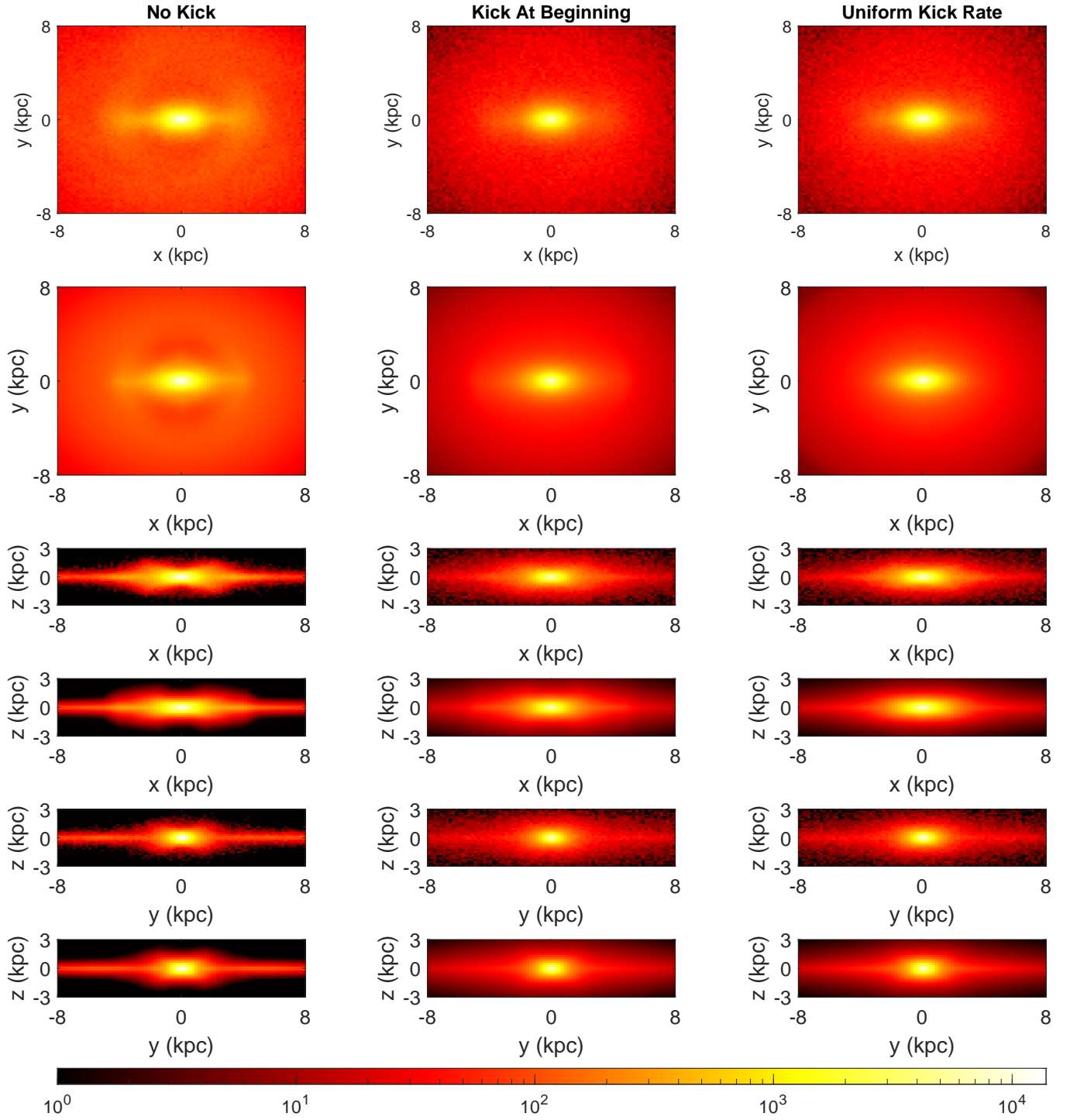


Figure A.1. Final density map of particles with no kick, a kick at the beginning and a uniform kick rate generated from the MWb initial conditions. Every second row shows the fitted model.

A Uniform kick rate, MWb, and MWc0.8 figures

As the uniform kick rate, MWb, and MWc0.8 gave similar results to the MWa kicked at beginning case we have moved many of their figures to this appendix.

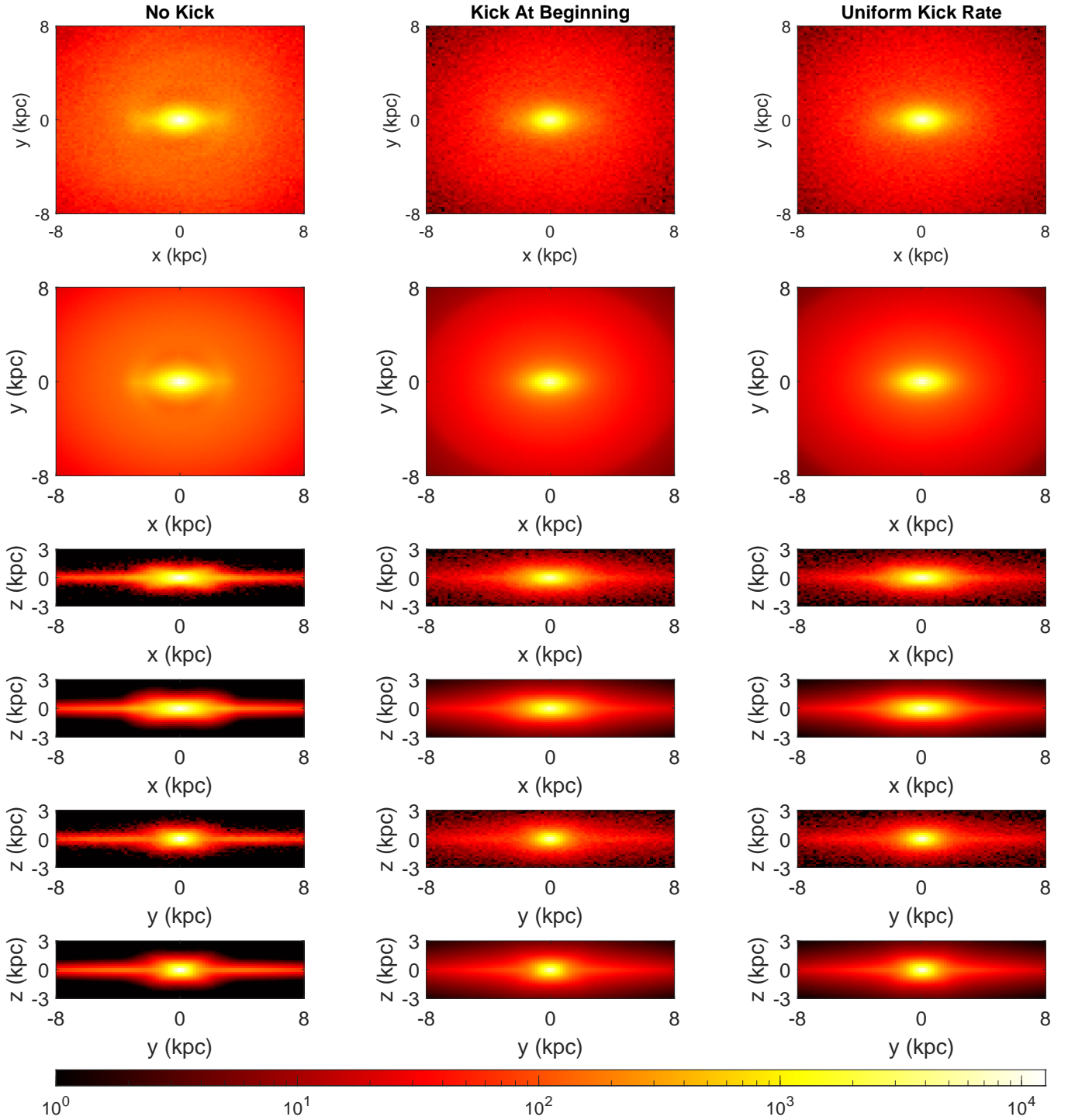


Figure A.2. Final density map of particles with no kick, a kick at the beginning and a uniform kick rate generated from the MWc0.8 initial conditions. Every second row shows the fitted model.

B Markov Chain Monte Carlo Method

In previous work, such as ref. [30], we used for our MCMC the adaptive Metropolis algorithm of Haario et al. [56]. In this article, however, we found it was necessary to replace adaptive Metropolis algorithm with an alternative algorithm to ensure rapid convergence to the peak likelihood region of the parameter space. The MCMC algorithm used in this article is similar to that of Foreman-Mackay et al. [43] with a mixture of the Differential Evolution [44] and snooker updates [45]. Instead of performing a single random walk through the parameter space where proposed moves are accepted with a probability based on the likelihood of the current point of the chain and the proposed next point,

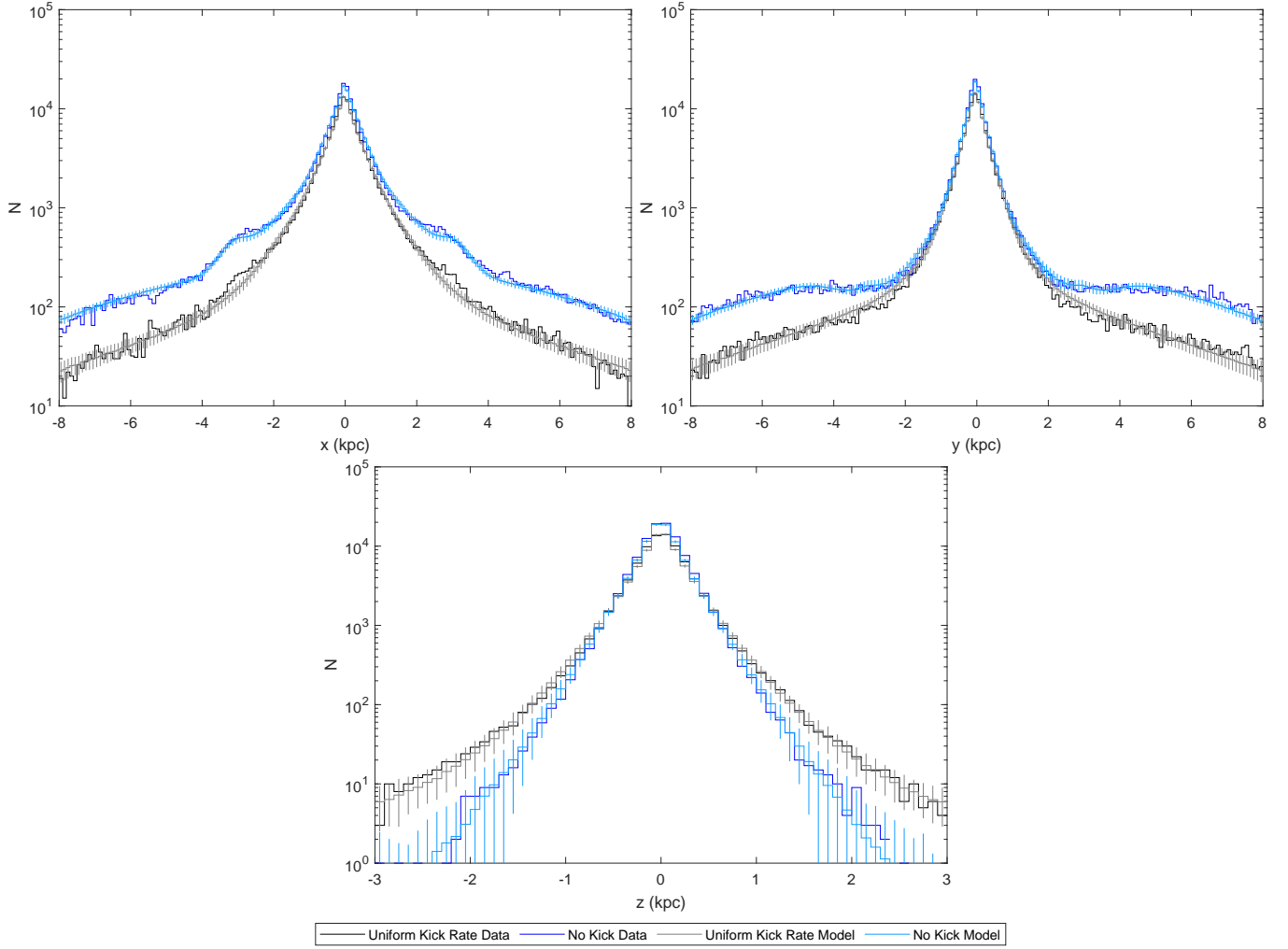


Figure A.3. Final profile along x , y and z axes with a uniform kick rate generated from the MWa initial conditions. We show both N -body simulation data and data simulated using the fitted model. For the fitted model we show the mean number of particles in each bin and the standard deviation.

we use an ensemble of K “walkers” where a proposed update for a walker j depends on the distribution of the other walkers.

A single step of the stretch move update suggested in Foreman-Mackay et al. [43] involves updating the K walkers sequentially. Let \mathbf{x}_j be the state of walker j , an update for walker \mathbf{x}_j is performed as follows:

1. Draw k from $1, 2, \dots, K$ where $k \neq j$
2. Draw z from the probability density function with parameter a (Foreman-Mackay et al. [43] suggest $a = 2$):

$$g(z) \propto \begin{cases} \frac{1}{\sqrt{z}} & z \in [\frac{1}{a}, a] \\ 0 & \text{otherwise} \end{cases} \quad (\text{B.1})$$

3. Calculate proposal $\mathbf{y} = \mathbf{x}_k + z(\mathbf{x}_j - \mathbf{x}_k)$
4. Calculate acceptance probability r :

$$r = z^{d-1} \frac{p(\mathbf{y})}{p(\mathbf{x}_j)} \quad (\text{B.2})$$

where d is the number of dimensions

5. Set $\mathbf{x}_j = \mathbf{y}$ with probability $\min(1, r)$

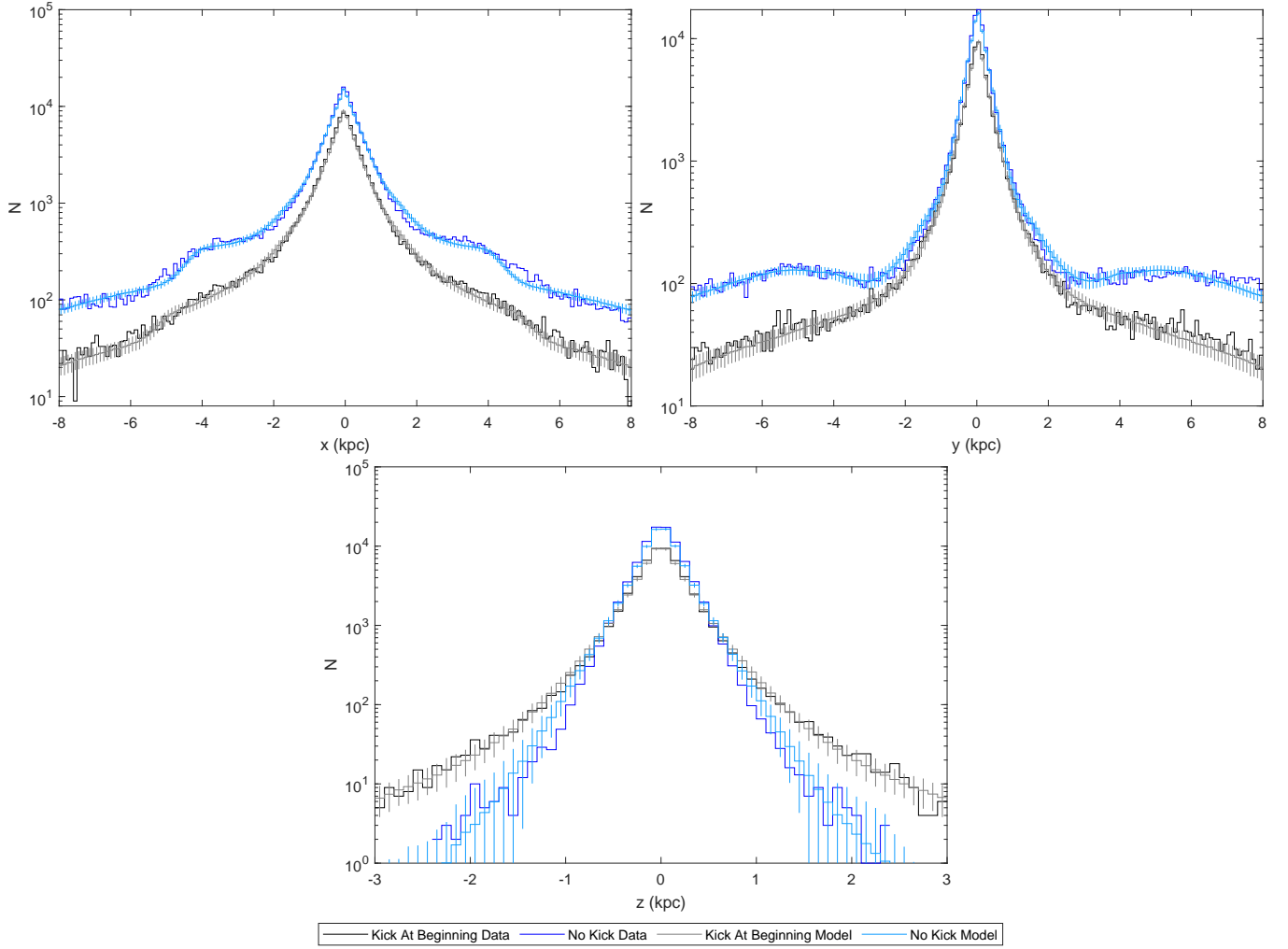


Figure A.4. Final profile along x , y and z axes with kicks occurring at the beginning generated from the MWb initial conditions. We show both N -body simulation data and data simulated using the fitted model. For the fitted model we show the mean number of particles in each bin and the standard deviation.

We found better results using a mixture of two alternative updates: 80% the Differential Evolution update of ter Braak [44] and 20% the snooker update of ter Braak and Vrugt [45].

To update walker \mathbf{x}_j using the Differential Evolution update:

1. Draw k and l from $1, 2, \dots, K$ where $k \neq j$, $l \neq j$ and $l \neq k$
2. Propose $\mathbf{y} = \mathbf{x}_j + \gamma(\mathbf{x}_k - \mathbf{x}_l) + \mathbf{e}$ where γ is a parameter and where \mathbf{e} is drawn from a small d dimensional symmetric probability distribution
3. Calculate acceptance probability r :

$$r = \frac{p(\mathbf{y})}{p(\mathbf{x}_j)} \quad (\text{B.3})$$

4. Set $\mathbf{x}_j = \mathbf{y}$ with probability $\min(1, r)$

We drew \mathbf{e} from a d dimensional Gaussian with standard deviation 10^{-5} in each dimension. In case the likelihood distribution had multiple modes, we used $\gamma = 1$ with probability 0.1 as suggested by ter Braak [44], otherwise we used the default value of $\gamma = 2.38/\sqrt{2d}$.

Using the snooker update, we update \mathbf{x}_j as follows:

1. Draw k , l and m from $1, 2, \dots, K$ with no index repeated or equal to j

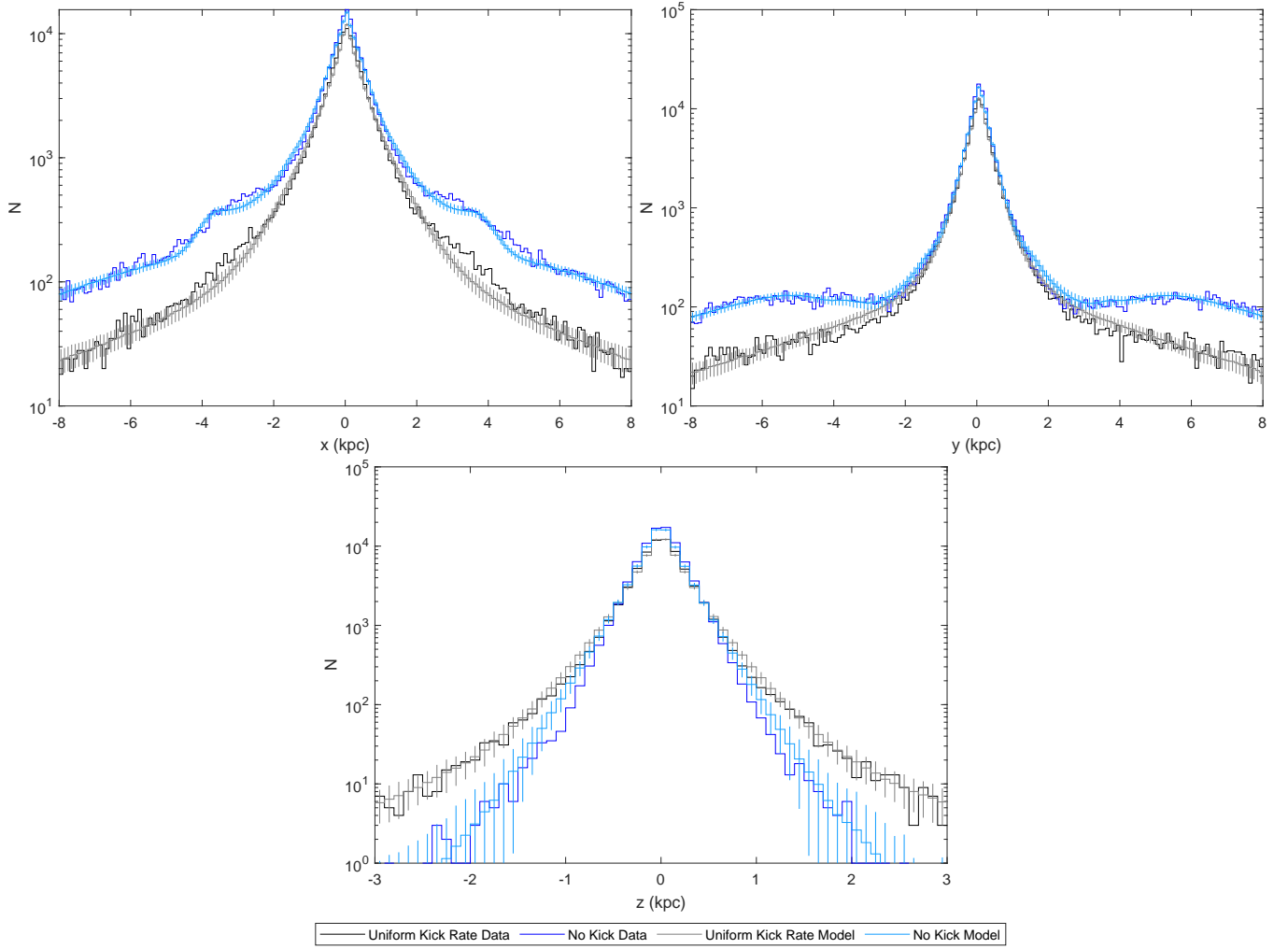


Figure A.5. Final profile along x , y and z axes with a uniform kick rate generated from the MWb initial conditions. We show both N -body simulation data and data simulated using the fitted model. For the fitted model we show the mean number of particles in each bin and the standard deviation.

2. Calculate the orthogonal projections of \mathbf{x}_l and \mathbf{x}_m onto the line $\mathbf{x}_j - \mathbf{x}_k$, $\text{proj}_{\mathbf{x}_j - \mathbf{x}_k}(\mathbf{x}_l)$ and $\text{proj}_{\mathbf{x}_j - \mathbf{x}_k}(\mathbf{x}_m)$, where:

$$\text{proj}_{\mathbf{u}}(\mathbf{v}) = \frac{\mathbf{v} \cdot \mathbf{u}}{\mathbf{u} \cdot \mathbf{u}} \mathbf{u} \quad (\text{B.4})$$

3. Propose $\mathbf{y} = \mathbf{x}_j + \gamma_s \left(\text{proj}_{\mathbf{x}_j - \mathbf{x}_k}(\mathbf{x}_l) - \text{proj}_{\mathbf{x}_j - \mathbf{x}_k}(\mathbf{x}_m) \right)$ where γ_s is a parameter

4. Calculate acceptance probability r :

$$r = \frac{p(\mathbf{y}) |\mathbf{y} - \mathbf{x}_k|^{d-1}}{p(\mathbf{x}_j) |\mathbf{x}_j - \mathbf{x}_k|^{d-1}} \quad (\text{B.5})$$

5. Set $\mathbf{x}_j = \mathbf{y}$ with probability $\min(1, r)$

We use $\gamma_s = 2.38/\sqrt{2}$ as suggested by ter Braak and Vrugt [45].

We also used a simple annealing method in which we divide the log-likelihood by a temperature T which is gradually reduced to 1. The posterior probability density for a parameter set θ at MCMC iteration t is:

$$p(\theta | N\text{-body data}) \propto p(\theta) L^{1/T_t} \quad (\text{B.6})$$

where $p(\theta)$ is the prior, L is the likelihood, and T_t is the temperature. We used a linearly decreasing $\log(T)$ from $\log(1000)$ to $\log(1)$ during the first half of each Markov chain, which we discard. This method allows the algorithm

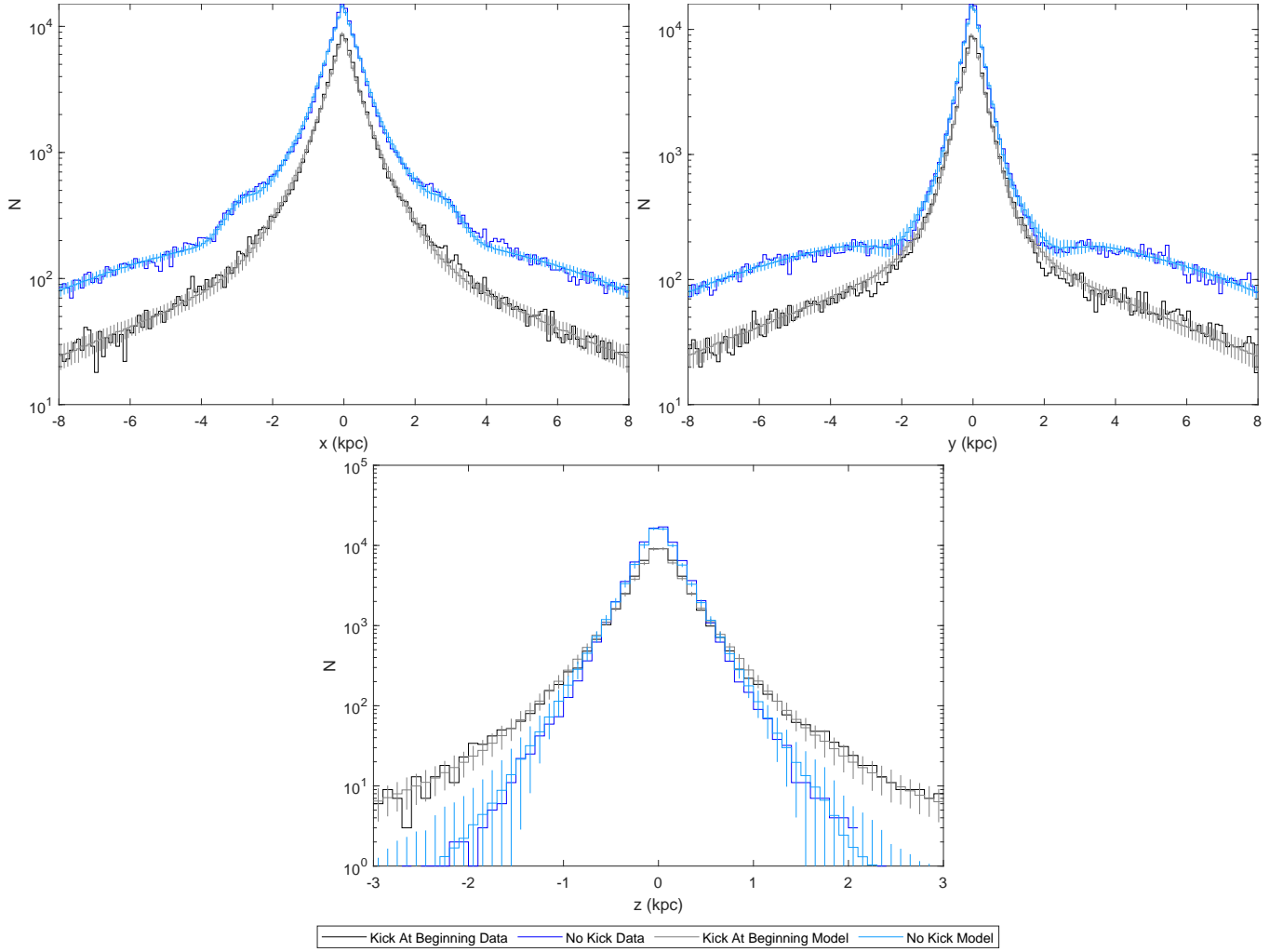


Figure A.6. Final profile along x , y and z axes with kicks occurring at the beginning generated from the MWc0.8 initial conditions. We show both N -body simulation data and data simulated using the fitted model. For the fitted model we show the mean number of particles in each bin and the standard deviation.

to explore a broad region in the parameter space, while slowly converging to the desired posterior distribution where $T = 1$. This appeared to help the Markov chains avoid getting stuck in local likelihood maxima.

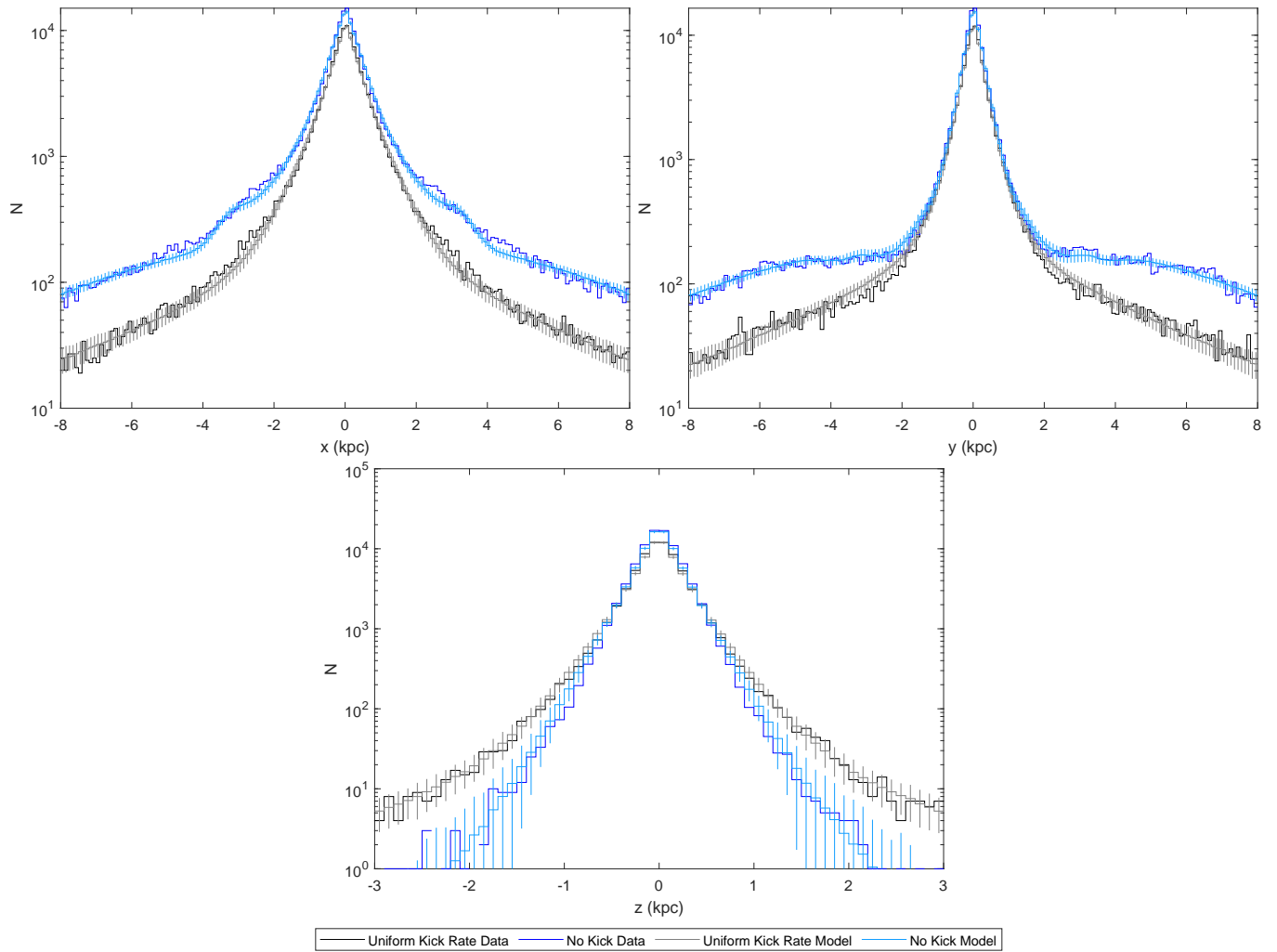


Figure A.7. Final profile along x , y and z axes with a uniform kick rate generated from the MWc0.8 initial conditions. We show both N -body simulation data and data simulated using the fitted model. For the fitted model we show the mean number of particles in each bin and the standard deviation.

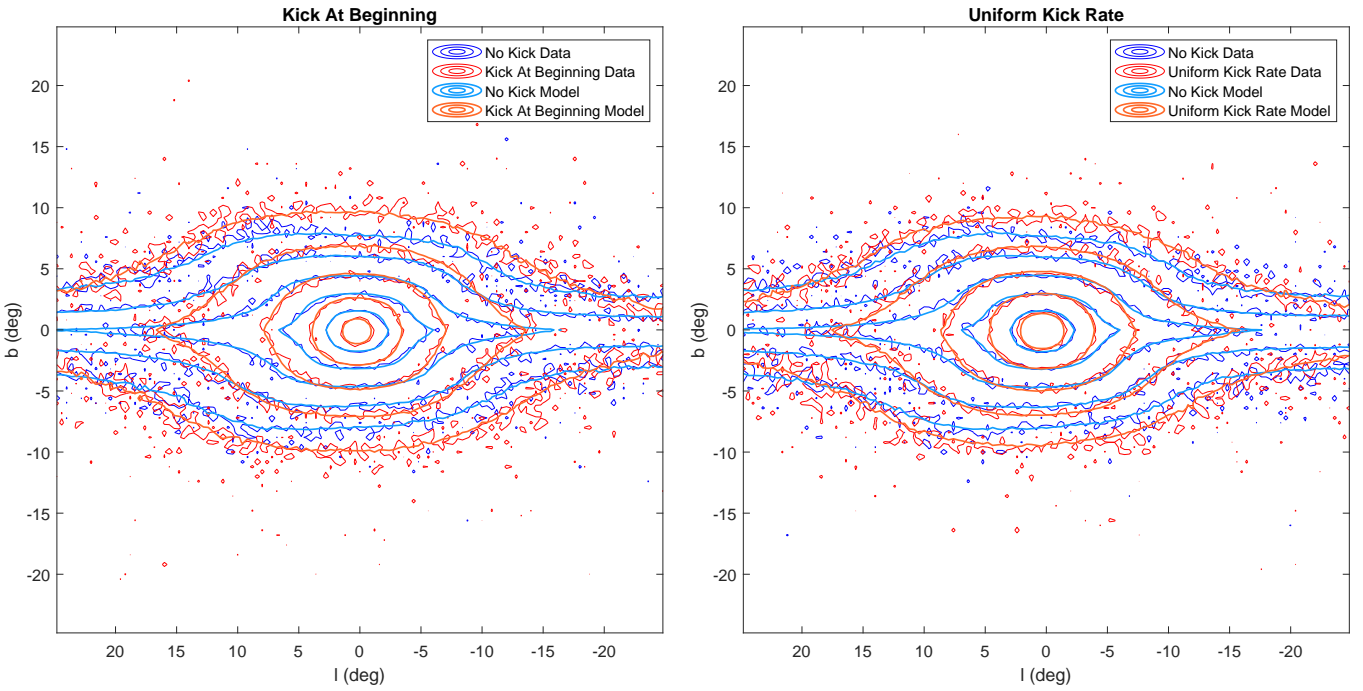


Figure A.8. Final flux distribution in Galactic coordinates generated from the MWb initial conditions. The contours for each distribution are at 1, 2, 4, 8 and 16 times the mean in this region. The Sun is placed at a distance of 7.9 kpc, at an angle relative to the bar of 20° and at a height of 15 pc.

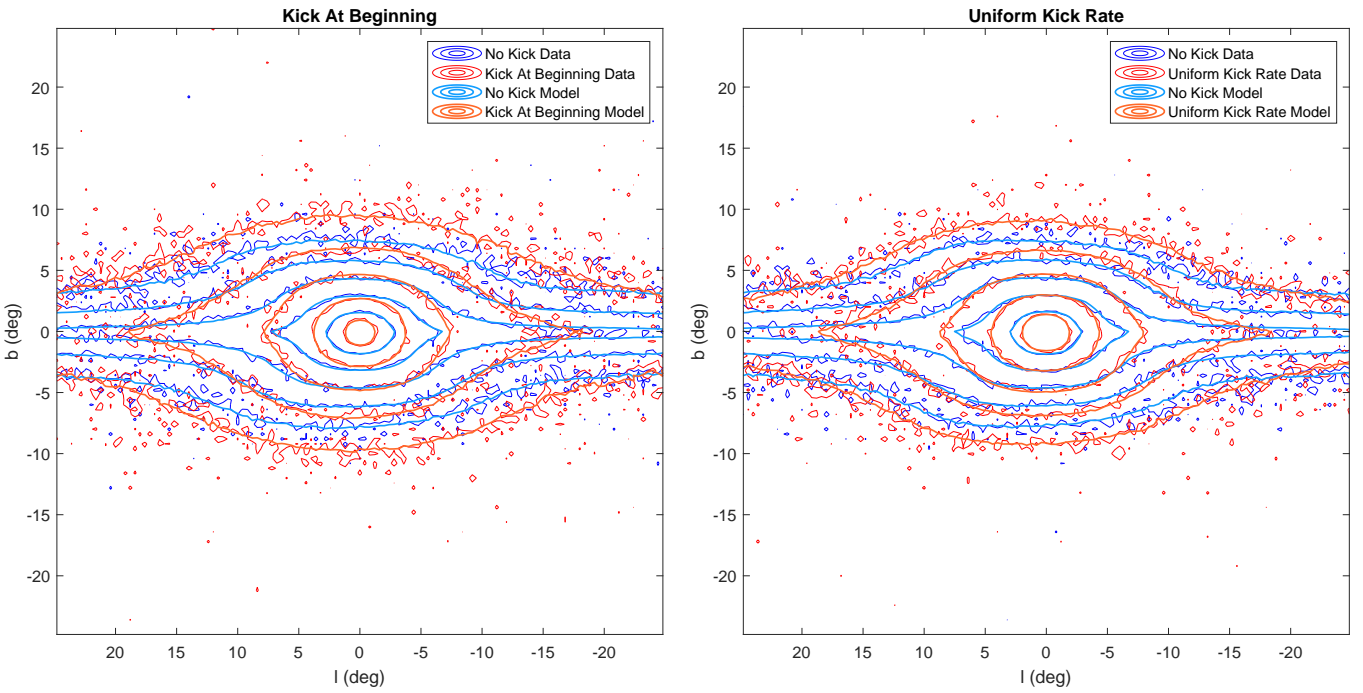


Figure A.9. Final flux distribution in Galactic coordinates generated from the MWc0.8 initial conditions. The contours for each distribution are at 1, 2, 4, 8 and 16 times the mean in this region. The Sun is placed at a distance of 7.9 kpc, at an angle relative to the bar of 20° and at a height of 15 pc.

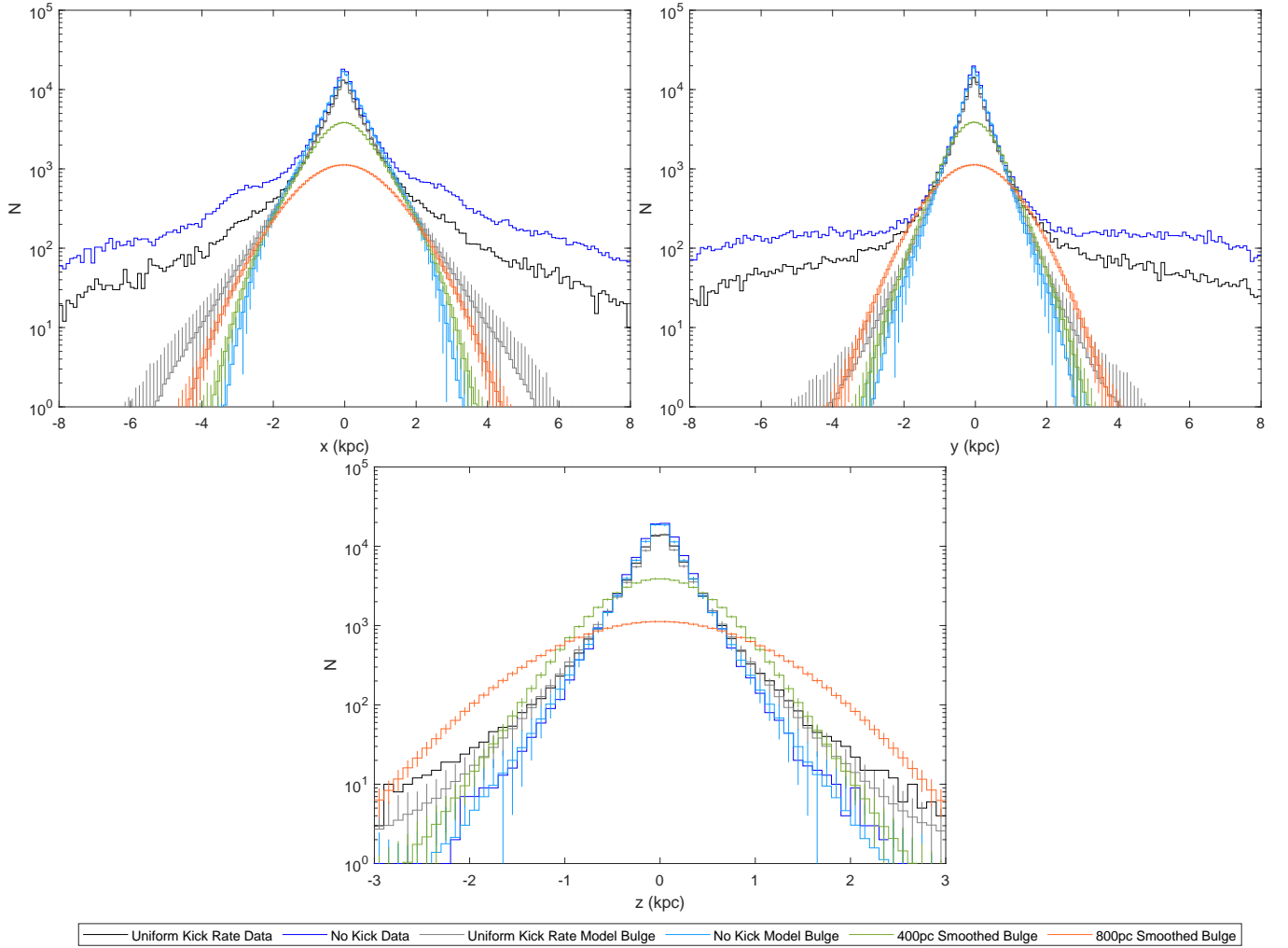


Figure A.10. Final profile along x , y and z axes with a uniform kick rate generated from the MWa initial conditions. Here we show the fitted bulge components, consisting of the bar plus Hernquist bulge, as well as the no kick bulge smoothed with 400 pc and 800 pc Gaussians. We show both N -body simulation data and data simulated using the fitted model. For the fitted model we show the mean number of particles in each bin and the standard deviation.

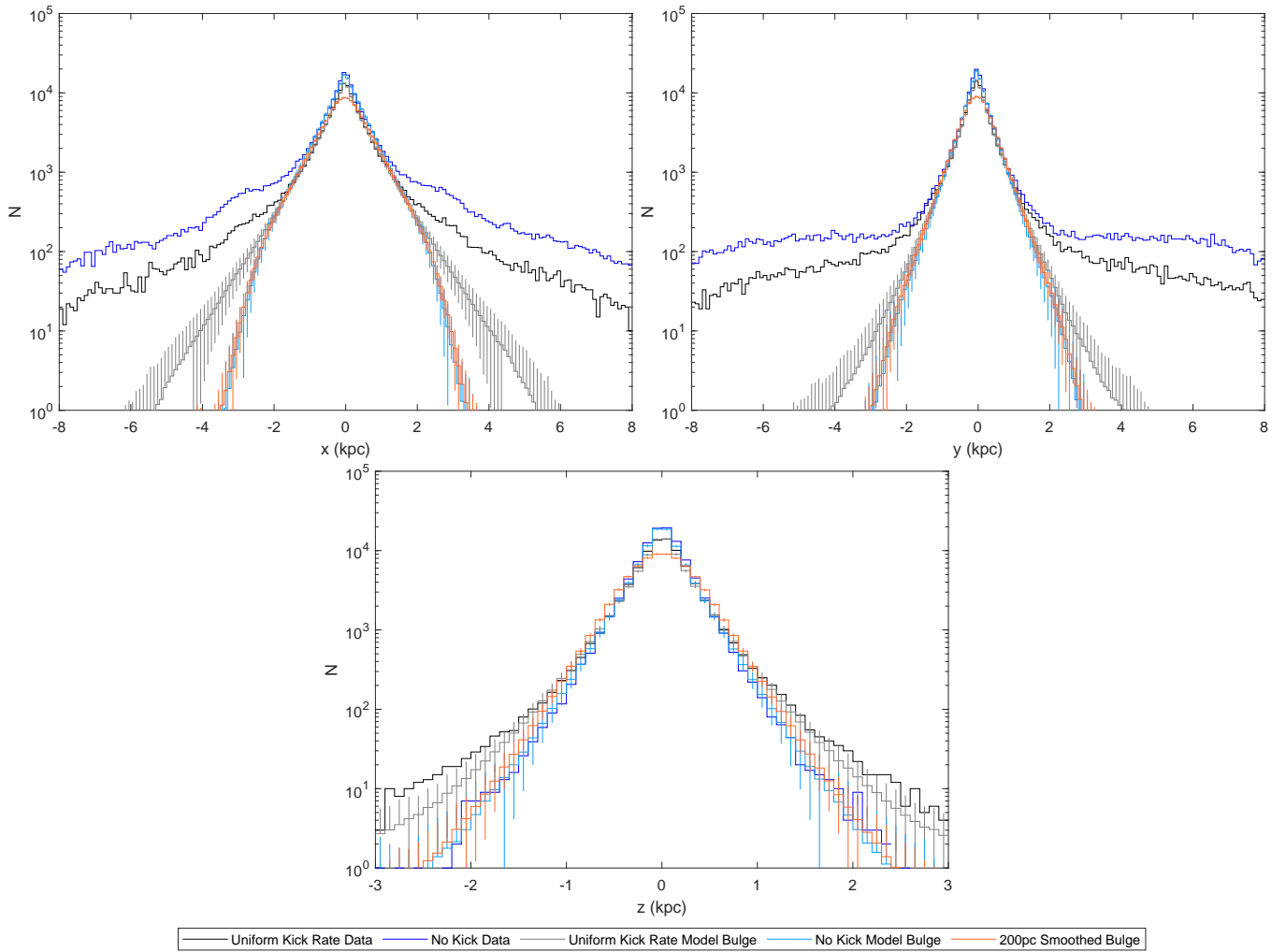


Figure A.11. Final profile along x , y and z axes with a uniform kick rate generated for the MWa initial conditions. Here we show the fitted bulge components as well as the no kick bulge smoothed with a 200 pc Gaussian. We show both N -body simulation data and data simulated using the fitted model. For the fitted model we show the mean number of particles in each bin and the standard deviation.

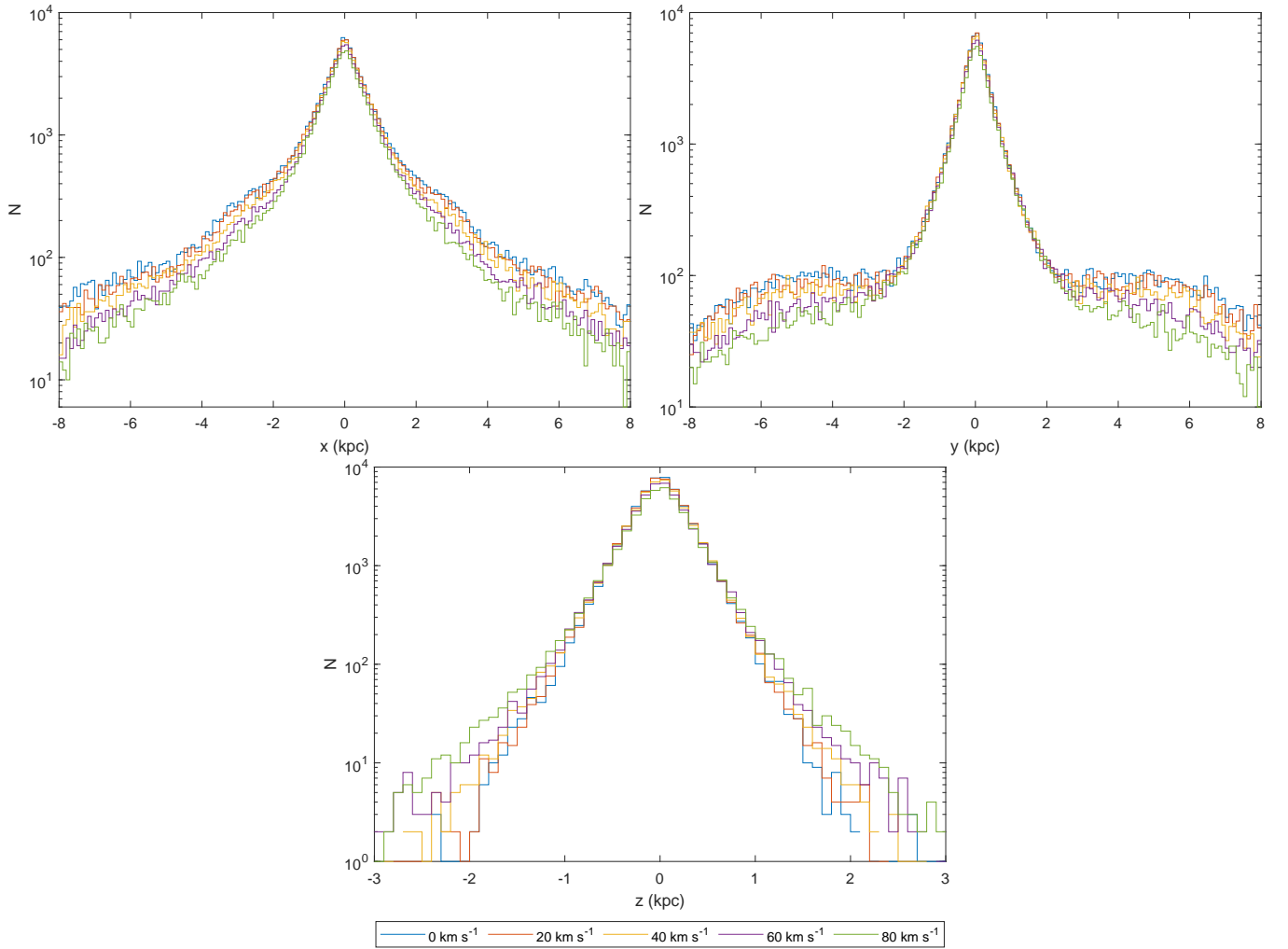


Figure A.12. Final profile along x , y and z axes with a uniform kick rate for kicks between 0 km s^{-1} and 80 km s^{-1} in 20 km s^{-1} increments. Generated from the MWA initial conditions.